Periodico di Mineralogia (2014), 83, 2, 257-297 DOI: 10.2451/2013PM0015

PERIODICO di MINERALOGIA
established in 1930

An International Journal of
MINERALOGY, CRYSTALLOGRAPHY, GEOCHEMISTRY, ORE DEPOSITS, PETROLOGY, VOLCANOLOGY
and applied topics on *Environment*, *Archaeometry* and *Cultural Heritage*

PT-path reconstruction via unraveling of peculiar zoning pattern in atoll shaped garnets via image assisted analysis: an example from the Santa Lucia del Mela garnet micaschists (northeastern Sicily-Italy)

Gaetano Ortolano[1,*], Roberto Visalli[1], Rosolino Cirrincione[1], Gisella Rebay[2]

[1]Università degli Studi di Catania, Dipartimento di Scienze Biologiche, Geologiche e Ambientali, Corso Italia 57, I-95129 Catania (Italy)
[2]Università degli Studi di Pavia, Dipartimento di Scienze della Terra e dell'Ambiente, Via Ferrata 1, 27100 Pavia (Italy)
[*]Corresponding author:*ortolano@unict.it*

Abstract

Garnet micaschists nearby Santa Lucia del Mela - Peloritani Mountains (North-eastern Sicily, Italy), were studied by integrating information obtained from petrographic and image-assisted analyses of mineral phase compositions by using X-ray maps and thermodynamic modeling. These rocks are characterized by the presence of atoll garnets, and preserve a continuous array of textures from pristine garnets, through peninsula or island textures, to atoll textures. Completely substituted garnets represent the final stage of the process. These textures result from the metamorphic evolution of the rocks, consisting of two main stages of recrystallization-deformation events. The sequence of mineral parageneses associated to successive deformation events is as follows: early D1 is characterized by the assemblage wm1 + chl1 + bt1 + pl1 + grt1 + qtz + ilm + ap; late D1 by grt2 + wm2 + chl2+ bt2 + pl2 + qtz + ilm + ap + hem; D2 (associated to garnet core transformation) by grt3 + bt3 + pl3 + wm3 + qtz + chl3 + ilm. On the basis of textural observations and mineral parageneses, the atoll formation is related to the substitution of garnet cores during the D2 stage, with the consumption of garnet cores (grt1) and production of new garnet rim (grt3) with wm, bi, qtz and pl. The recognition of the different stages of garnet growth and associated parageneses has been obtained using image analysis coupled with compositional maps, performed via multivariate statistical analysis of four selected X-Ray map arrays. Following the textural and mineral-chemical analyses, PT conditions associated to the three recrystallisation stages have been determined via pseudosection computations. Results indicate that the analyzed rock-types have recorded a clock-wise PT trajectory during the Variscan orogeny, defined by a prograde evolution, in amphibolite facies conditions, preserved in relic garnet cores, followed by an initial decompressional evolution toward lower amphibolite facies conditions associated

to a partial heating. During this last stage the multi stadial atollization process took place, retrogradely evolving toward a green-schist facies conditions, constrained through the compositions of the pseodomorphyc mineral aggregates gradually substituting previously formed garnets.

Key words: X-Ray Map Analyzer; Thermodynamic modeling; Perple_X; Southern Calabrian Peloritani Orogen.

Introduction

Petrological investigations of zoned crystals have played a key role in obtaining information on the mineral-chemical equilibria developed during the multistage P-T evolution of metamorphic rocks. For this purpose garnet is one of the most suitable mineral since, due to its slow cationic diffusion, is able to preserve shells with an original chemical composition (Ague and Carlson, 2013), often accompanied by a rapid growth after nucleation, allowing the inclusion of syn-kinematically matrix minerals. Since the pioneering work of Hollister (1966) and Tracy (1982), growth zoning pattern analyses have been widely used to reconstruct prograde and retrograde P-T history (Arenas et al., 1997; Cheng et al., 2007; Evans, 2004; Zuluaga et al., 2005; Cirrincione et al., 2008; Robyr et al., 2009; Angì et al., 2010; Faryad et al., 2010; Ruiz Cruz, 2011). One of the most rapid methods to highlight the chemical zoning patterns of minerals has been the use of X-ray maps. In this way, besides qualitative images to be combined with quantitative spot mineral-data, the possible presence of chemical gradients are individuated and quantified. More recently digital image analysis has been improved with the development of several software packages dedicated to image processing (e.g. Cossio and Borghi, 1998; Cossio et al., 2002; Flesche et al., 2000; De Andrade et al., 2006; Fryel and Lyman, 2006; Lanari et al., 2014). These improvements, recently directly implemented in the modern micro-analytical devices, only in part allow the extrapolation of quantitative information from multispectral image analysis, such as X-ray maps. Moreover, these software are often characterized by high implementation costs involved by the needed time consuming training. In this view, the recent development of a new user-friendly GIS-based image-processing procedure (i.e. X-Ray Micro Analyzer - Ortolano et al., 2014), makes affordable a multivariate statistical analysis of X-ray maps (Launeau et al., 1994; Bonnet, 1995, 1998). This procedure is useful in deciphering quantitative textural and modal parameters from selected thin section micro-domains, contributing to minimize the subjectivity of the operator in determining the effective equilibrium paragenesis. For instance, it makes possible to evidence zoning patterns that may be due to fractionation (e.g. Fiannacca et al., 2012). The use of this tool allows to distinguish and to quantitatively determine different compositional regions within a rock or mineral that are linked to the sequential mineral growth stages occurring during metamorphism. Moreover it provides

essential compositional information to constrain the P-T evolution via pseudosection calculations using equilibrium thermodynamic based software (Holland and Powell, 1998; Connolly and Petrini, 2002; Connolly, 2005; de Capitani and Petrakakis, 2010). In the following, the chemical zoning of atoll garnets from Santa Lucia del Mela zone (northeastern Sicily, Italy) will be subjected to image analysis.

The atoll texture is a particular kind of corona texture consisting of a garnet ring surrounding an aggregate of mineral phases, usually quartz, micas, plagioclase and Fe oxides (Passchier and Trouw, 1998). Despite various studies on atoll garnets (Atherton and Edmunds, 1966; Cooper, 1972; Smellie, 1974, 1989; Spiess et al., 2001; Dobbs et al., 2003; Homam, 2003, 2006; Cheng et al., 2007; Faryad et al., 2010; Ruiz Cruz, 2011; Hibraim, 2012; Robyr et al., 2014), the genetic mechanisms and the conditions of formation of these peculiar structures have not yet been unambiguously defined. Several models have been proposed in different geologic contexts, such as selective replacement (Smellie, 1974; Homam, 2003, 2006; Cheng et al., 2007; Faryad et al., 2010), rapid poikiloblastic growth (Atherton and Edmunds, 1966), multiple nucleation and coalescence processes (Spiess et al., 2001; Dobbs et al., 2003) and, finally, a change in the stoichiometry of the reactions that lead to the transition from a poykilitic core to an euhedral rim devoid of inclusions (Robyr et al., 2014). Nevertheless, the possibility of identifying the simultaneous activity of different mechanisms is not rare (Ruiz Cruz, 2011).

The aim of this work is to use quantitative textural data, obtained from image-assisted analysis of four selected garnet domains relatable to different stages of "*atollization"* process, in order to reconstruct the sequential order of crystallization of this peculiar texture from upper green-schist facies to amphibolite facies in metapelites outcropping in the northern part of the Peloritani Mountains. The results are also useful to ascertain which one of the atollization mechanisms suggested in the literature can be invoked in this case, and to constrain the different stages of recristallization undergone by the selected samples during their PT evolution, witnessed by this relic portion of the southern European Variscan Chain (Cirrincione et al., 2012). This last analysis, associated with the integration of microstructural investigations, has been executed by thermodynamic modeling via PT pseudosection calculation using the software Perplex (Connolly and Petrini, 2002; Connolly, 2005).

Geological setting

Samples characterized by the presence of atoll garnets come from the area of Santa Lucia del Mela, Peloritani Mountains (North-eastern Sicily), a portion of the southernmost part of Calabrian-Peloritani Orogen (CPO), which represents the innermost tectonic element of the Apennine-Maghrebian orogen and geographically extends from the north of Calabria to the northeast of Sicily (Figure 1 a,b), to continue up to the Betic-Rif belt. In its crystalline basement units, this orogenic segment preserves evidence of a polyorogenic multistadial evolution resulting

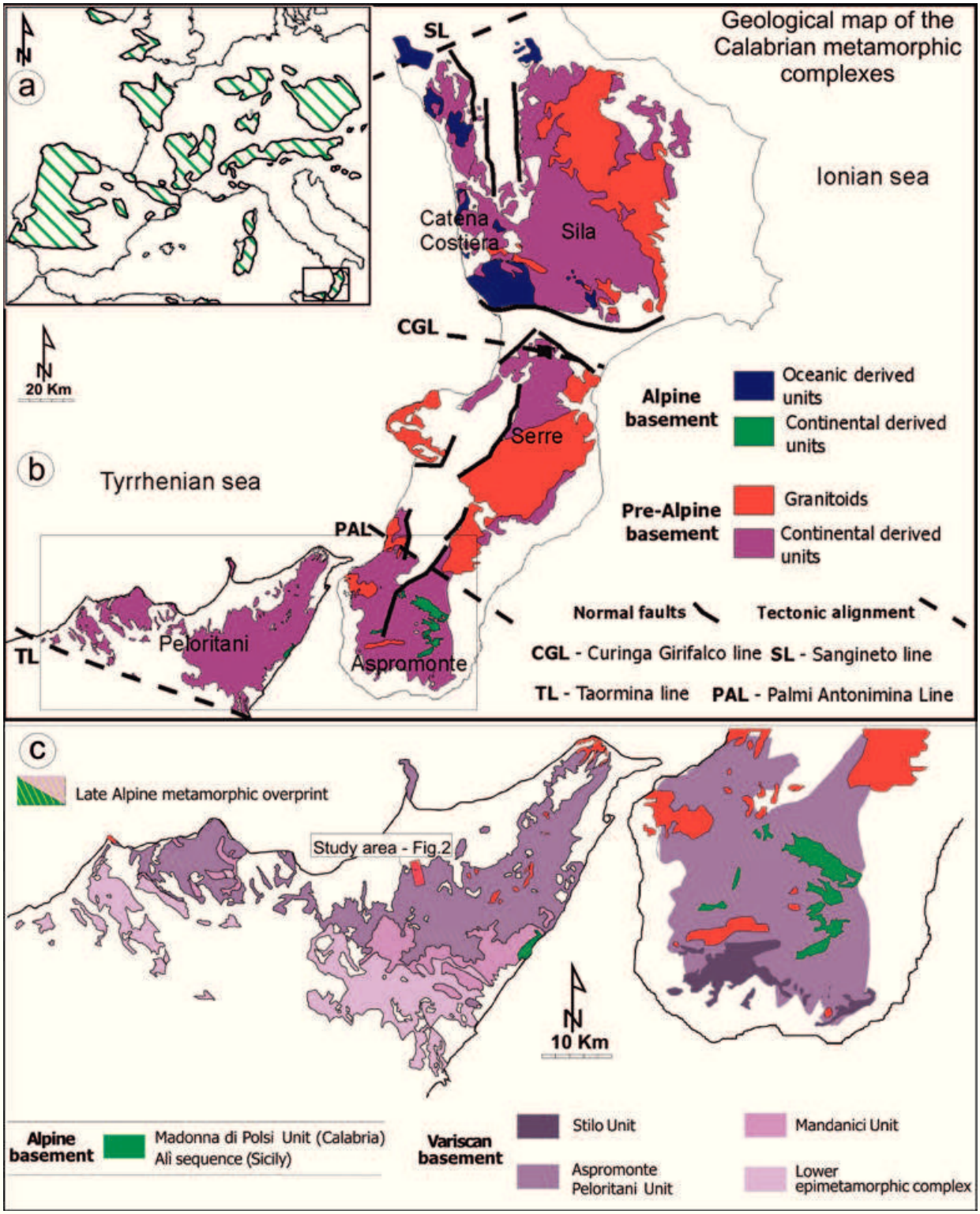

Figure 1. Regional geological framework of the study area: a) Distribution of Variscan relict metamorphic basements in Europe, after von Raumer, 2002; b) Geological map of the Calabrian metamorphic complexes, after Angì et al., 2010; c) Geological sketch map of the Peloritani Mountains and Aspromonte Massif crystalline basement complexes with the subdivision of the tectono-metamorphic units (after Cirrincione et al., 2012, modified).

from the Alpine reworking of original late-Paelozoic (i.e. Variscan orogeny) (Cirrincione et al., 2008, 2012) or possibly older (De Gregorio et al., 2003; Ferla, 2000; Messina et al., 2004) basement rocks.

From a physiographic point of view, the CPO is constituted by the north-south trending domain composed by the Catena Costiera and Sila (i.e. Northern CPO), and by the NE-SW trending alignment of the Serre-Aspromonte Massif (Calabria), which continues in Sicily with the E-W trending orogenic belt of the Peloritani Mountains (i.e. Southern CPO, Cirrincione et al., 1999; Piluso et al., 2000; Cella et al., 2004; Festa et al., 2004) (Figure 1b). According to Cirrincione et al. (1999, 2012) the Peloritani Mountains can be described as a nappe-pile subdivided into a Lower and an Upper Complex (Figure 1c). The Lower Complex includes three tectonic units (the Capo S. Andrea Unit, the Longi Taormina Unit and the S. Marco d'Alunzio Unit, from bottom to top) cropping out in the southern part of the Peloritani Mountains. These units consist of late-Paelozoic very low-grade basement rocks that have a Mesozic-Caenozoic continental margin sedimentary cover with no Alpine metamorphic overprint. The overlying units, belonging to the Upper Complex, consist of two main overturned tectonic slices, comprehensive of low to medium-high grade Variscan metamorphic rocks (the Mandanici and Aspromonte-Peloritani Units), which have an Alpine metamorphic overprint. The rocks belonging to the Mandanici Unit are low-grade phyllites, crystalline limestones, phyllitic schists, greenschists and interbedded quartzites affected by a Variscan polyphase metamorphism from upper greenschist- to lower amphibolites-facies (T = 550 °C, P = 2-3 kbar; Atzori and D'Amico, 1972; Cirrincione and Pezzino, 1991; Ferla, 2000). The Aspromonte-Peloritani Unit outcrops also in the Aspromonte Massif (southern Calabria), devoid of Mesozoic sedimentary cover. This unit consists of medium to high-grade amphibolite facies metamorphic rocks: paragneisses, ortho-derived augen gneisses and minor micaschists, amphibolites and marbles characterised by an amphibolites facies Variscan-type polyphase metamorphism (Pezzino et al., 1990; Puglisi and Pezzino, 1994; Cirrincione et al., 2008). These terranes have been subsequently intruded by late Hercynian granitoids (315-290 Ma, Rb/Sr ages; Rottura et al., 1990; Fiannacca et al., 2008) when a widespread late-Paeleozoic temperature increase took place. This evolution was followed by an Alpine multistage overprint, preserved along the contact with the underlying Mandanici Unit. The atoll garnet-bearing samples were collected from some outcrops located 6 Km south-east from the town of Santa Lucia del Mela in the area between the Mela and Floripotema rivers belonging to the Aspromonte-Peloritani Unit (Figure 2).

Methodological approach

A preliminary microstructural analysis by means of optical microscope has been performed on about twenty thin sections in order to recognize the textural relationships, and the associated mineral parageneses, in which a

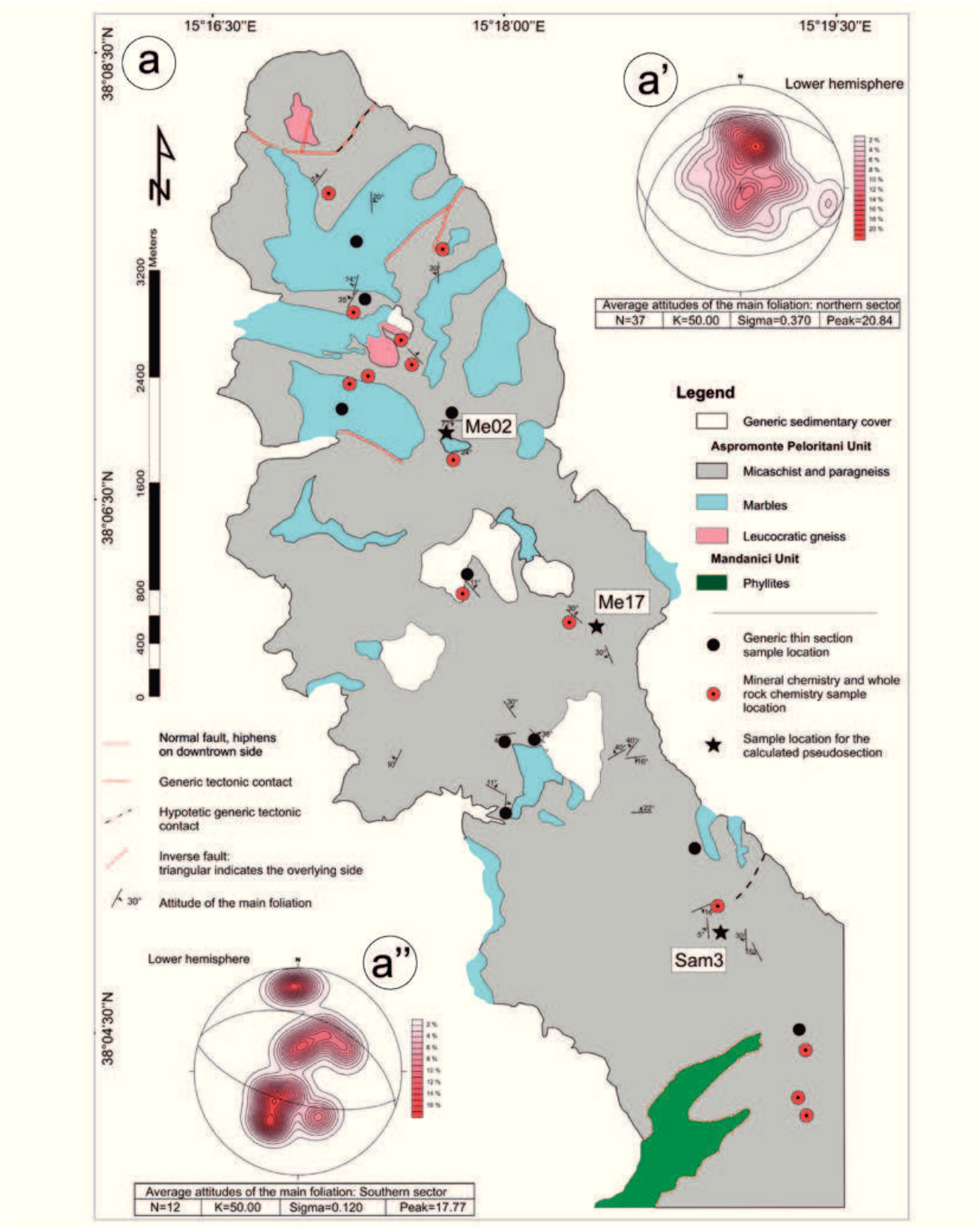

Figure 2. a) Geological sketch map of the study area with sample location: b') and b'') stereoplots of the northern and southern plane poles of the main foliation with relative average planes (S2).

reconstruction of the history of the blasto-deformational sequence recorded by the analyzed samples can be grounded.

Such an investigation was integrated by the determination of the whole-rock chemical analyses (Table 1), in order to obtain the composition of the equilibrium volume relative to the early metamorphic stages, used for the calculation of the P-T pseudosections. Bulk rock chemistry was obtained by XRF on pressed powder pellets using a Philips PW 2404 spectrometer equipped with a Rh anticathode at the Department of Biological, Geological and Environmental Sciences of Catania University. FeO/Fe_2O_3 ratio was determined by titration with $KMnO_4$; H_2O was measured as weight loss on ignition (L.O.I.) and was determined with standard gravimetric procedures, after heating the powder at ~ 900 °C for about 6 h.

Four garnet micro-domains representative of different atoll development were chosen on selected polished thin sections of three selected samples (Figure 2 - Table 2) and analyzed at the Laboratory of Electron Microscopy of Department of Biological, Geological and Environmental Sciences, University of Catania. Microanalytical data for major element abundances on garnet, plagioclase, ilmenite, biotite, white mica and chlorite (Appendix A) were obtained by means of a Tescan Vega-LMU scanning electron microscope equipped with an EDAX Neptune XM4-60 micro-analyzer operating by energy dispersive system characterized by an ultra-thin Be window coupled with an EDAX WDS LEXS (wavelength dispersive low energy X-ray spectrometer) calibrated for light elements. Operating conditions were 20 kV accelerating voltage and 0.2 nA beam current. Repeated analyses on internationally certified Alm-rich garnet, Na-rich plagioclase, biotite and glass inner standards during the analytical runs ensure precision for all the collected elements in the order of ± 3%. X-ray maps, useful to highlight compositional variations, were obtained on the same domains to derive Al, Ca, Fe, K, Mg, Mn, Na, Si and Ti distribution and concentration. These maps are 512*400 pixels and each pixel corresponds to about 2 μm per side. Maps were obtained with a dwell time of 500 ms per 128 frame, corresponding to an average acquisition time of 4 hours and 20 minutes. The results of the spot-chemical analyses have been processed by means of Minpet 2.02 software (Richard, 1985) to recalculate the formula of each mineral. Garnet formulae have been recalculated on the basis of 12 oxygens and 8 cations; micas on 24 oxygens and 12 cations, respectively, and feldspars on 8

Table 1. XRF Bulk rock composition of representative samples.

Sample	SiO_2	Al_2O_3	FeO_{tot}	MnO	MgO	CaO	Na_2O	K_2O	Total
Me 17	64.04	16.93	7.39	0.09	3.96	1.72	2.03	3.85	100
Sam 3	58.94	17.60	8.82	0.25	4.76	3.71	2.51	3.40	100

Table 2. Sample location and related paragenesis.

Sample	Coordinates*		Observed minerals	Litotype
	N	E		
Me 02	38° 07' 31''	15° 17' 13''	Qtz, Pl, Bt, Wm, Grt, Chl (Ilm, Sph, Ap, Rt)	Garnet micaschist
Me 17	38° 04' 57''	15° 19' 09''	Bt, Qtz, Wm, Pl, Grt, Chl (Ilm, Ap, Tur)	Garnet micaschist
Sam 3	38° 04' 33''	15° 19' 28''	Qtz, Pl, Bt, Wm, Grt, Chl (Ilm, Ap, Hem)	Garnet micaschist

* Coordinates were collected by GPS and are expressed according to the WGS84 system.

oxygens; all the iron was regarded as FeO.

The above routinely performed investigations were supported by a new software platform of image analysis (i.e. X-Ray Map Analyzer - XRMA, Ortolano et al., 2014) capable to generate graphical outputs useful for classifying chemically homogeneous zones as well as extracting quantitative textural information through the statistical data handling of X-ray maps. In the present research XRMA was used to evidence the compositional differences and the micro-textural relationships between, and within, individual mineralogical phases, possibly related to the different stages of P-T evolution (e.g. Fiannacca et al., 2012). To this aim, the X-ray maps of the four selected domains have been processed through the following two analytical cycles:

1) the first one consisted in the analysis of the entire selected domains, in order to recognize all the existing mineral phases. The principal component analysis (PCA), was followed by the image classification performed by means of a maximum likelihood classification (MLC) algorithm, which assigns to each pixel a specific arbitrary color. In this way a distribution mineral map was obtained, that allows to recognize micrometer mineral phases such as inclusion trails, thus defining textural relationships between mineral constituents in great detail (Appendix B);

2) the second one consisted in a further analysis of the previously recognized garnets in order to point out further potential subdivisions, such as those related to mineral zoning or those indicative of mineral reactions. To do this, the software offers two options: i) through the first one (sub-classification of mineral phases) a sub-zoning map of the garnet was obtained; ii) through the second one the density distribution of selected elements within garnet was obtained (Appendix B).

Finally P-T pseudosections, representing a total phase diagram section related to a specific bulk composition, were calculated with the Perplex software package (Connolly and Petrini, 2002; Connolly, 2005). The equilibrium volumes

of the former metamorphic evolutionary stages were determined using the XRF bulk compositions. Then, a modal based effective bulk rock chemistry determination, assisted by image analysis, has been derived to constrain the P-T evolution during the different stages of the atoll shaped garnet formation.

In this way it was possible to calculate the effective bulk rock chemistry for the retrograde PT steps, by applying a computational approach based on the volume percentage of the interpreted parageneses.

Petrography

Petrographic investigations have been focused on twenty thin sections of medium to fine grained garnet-mica-schists, characterized by an eterogranular anisotropic texture with a prevalent grano-lepidoblastic structure.

The sequence of the blasto-deformation events can be completely ascribed to the former up to the first retrograde stages of the Variscan metamorphic cycle. The first one (D1) brings to the formation of an axial plane schistosity (S1) along which a synkinematic assemblage given by wm1 + chl1 + bt1 + pl1 + grt1 + qtz + ilm crystallize during the earlier stage, followed by a later metamorphic stage given by grt2 + wm2 + chl2+ bt2 + pl2 + qtz + ilm + ap + hem (Figure 3).

The first stage evolves toward a non coaxial deformational (D2) which brings to the formation of the dominant foliation, represented by a well-developed schistosity (S2). This last

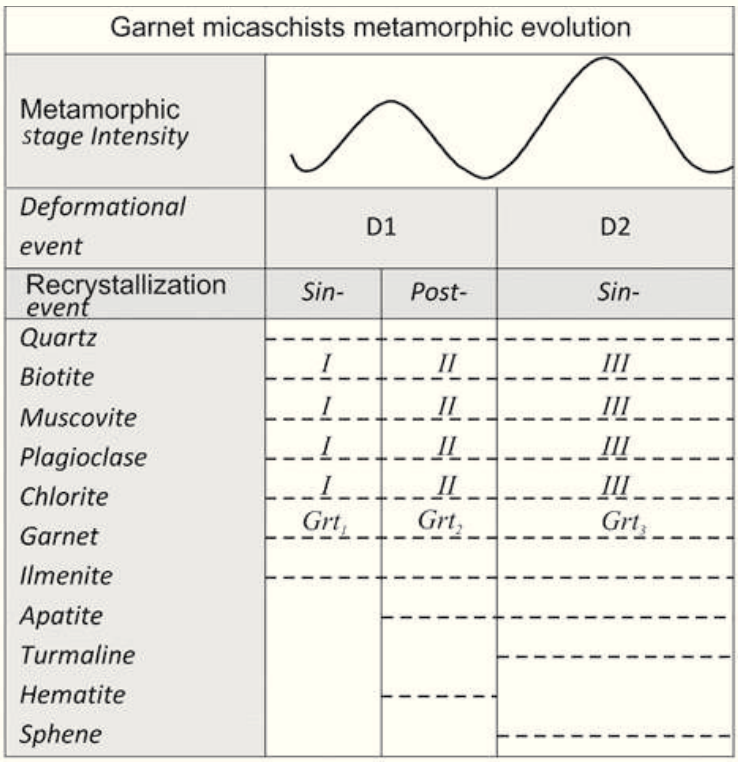

Figure 3. Synoptic representation of the deformation - recrystallization relationships.

deformational stage largely obliterates earlier schistosity (S1), presently highlighted by the occurrence of deformed relict biotite and white mica at high angle to S2 (Figure 4a) or by widespread relics of micro-fold hinges within microlithons, preserved as tight to isoclinal fold hinges (Figure 4b).

S2 is defined by the parallel arrangement of fine grained granoblastic layers of xenoblastic plagioclase and quartz grains with undulose extinction alternating with phyllosilicate-rich layers of biotite, with abundant zircon inclusions, and fine grained white mica. Locally accessory tourmaline also occurs. These layers wrap syn- to late-S1 garnet porphyroblasts, characterized by euhedral to sub-euhedral shape and ranging in size from 1 to 3 mm. They are often strongly altered and fractured, and most of them have cores with inclusion trails of quartz, white mica and locally chloritized biotite. Accessory small ilmenite crystals parallel to the main foliation (i.e. S2) or included in the core of garnet are also common, while syn- to late-S1 apatite and, at times, subordinate sub-euhedral hematite locally occurs, rarely accompanied by rutile, occurring as detrital relicts of the original protolith.

Locally, inclusion-rich garnet cores are partially to completely pseudomorphosed, with the formation of the atoll shaped garnets as a consequence of a retrograde breakdown reaction with formation of an association of grt3 + bt3 + pl3 + wm3 + qtz + chl3 + ilm + ap + sph (Figures 3,4c). The formation of this third garnet generation is preferentially concentrated along the main fractures of the almost integer garnets (Figure 5a) or in the inner- and outer-rim portion

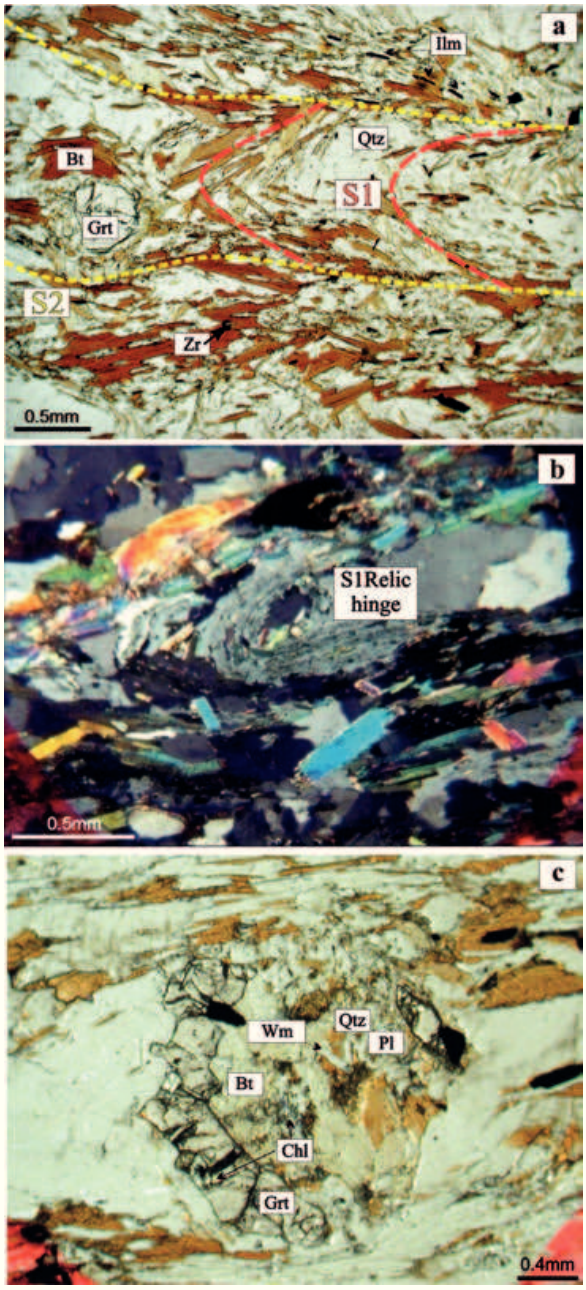

Figure 4. General description of garnet-micaschists microstructures. a) Fine grained granoblastic layers of xenoblastic plagioclase and quartz phyllosilicate-rich layers of biotite and white mica defining the main foliation (S2), with micro-fold hinges within microlithons testyfing an early schistosity (S1) (parallel polarizers). b) Deformed relict biotite and white mica at high angle to S2 in D1 fold hinges (crossed polarizers). c) Example of atoll shaped garnet characterized by a quasi complete euhedral garnet ring surrounding a core substituted by a biotite + muscovite + plagioclase + quartz + chlorite+ garnet3 aggregate.

of the advanced atoll shaped ones (Figure 5b). According to Faryad et al., (2010), these evidences suggest that the main mechanisms of atollization that can be invoked for our samples is the selective replacement of garnet cores, facilitated by the opening of fractures, instead of the others mechanism such as the rapid poikiloblastic growth (Atherton and Edmunds, 1966) or the multiple nucleation and coalescence processes (Spiess et al., 2001; Dobbs et al., 2003) as well as the change in the stoichiometry of the reactions during the transition from poykilitic garnet cores to euhedral rim devoid of inclusions (Robyr et al., 2014).

Four micro-domains identified in three of the collected samples (Table 2) have been chosen to further investigate the processes of formation of the atoll shaped garnet (Figure 6). The following selected micro-domains were considered as representative of the progressive stages of the atollization process: i) Me17, where different quantities of garnet substitution are found (from pristine garnet - Figure 6a) to almost completely corroded core (Figure 6c); ii) Sam3, where garnets cores are often preserved as a peninsula within the atoll (Figure 6b); and iii) Me02, where garnets are

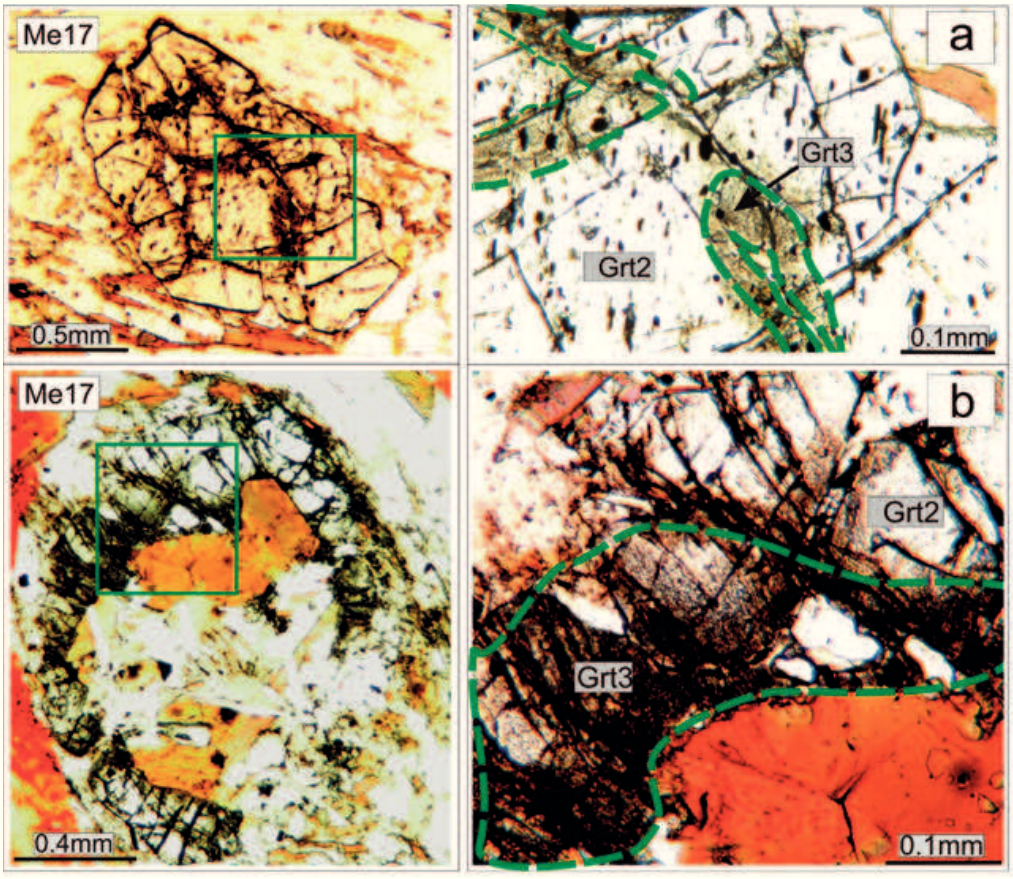

Figure 5. Examples of garnet zoning pattern: a) almost complete garnet characterized by two growing generations highlighted by an inclusion free garnet (grt2) replaced, along fractures, by garnet with cryptocrystalline inclusions (grt3) (parallel polarizers); b) second and third garnet generation preferentially crystallizing in the outer and inner rim position of the atoll ring, respectively (parallel polarizers).

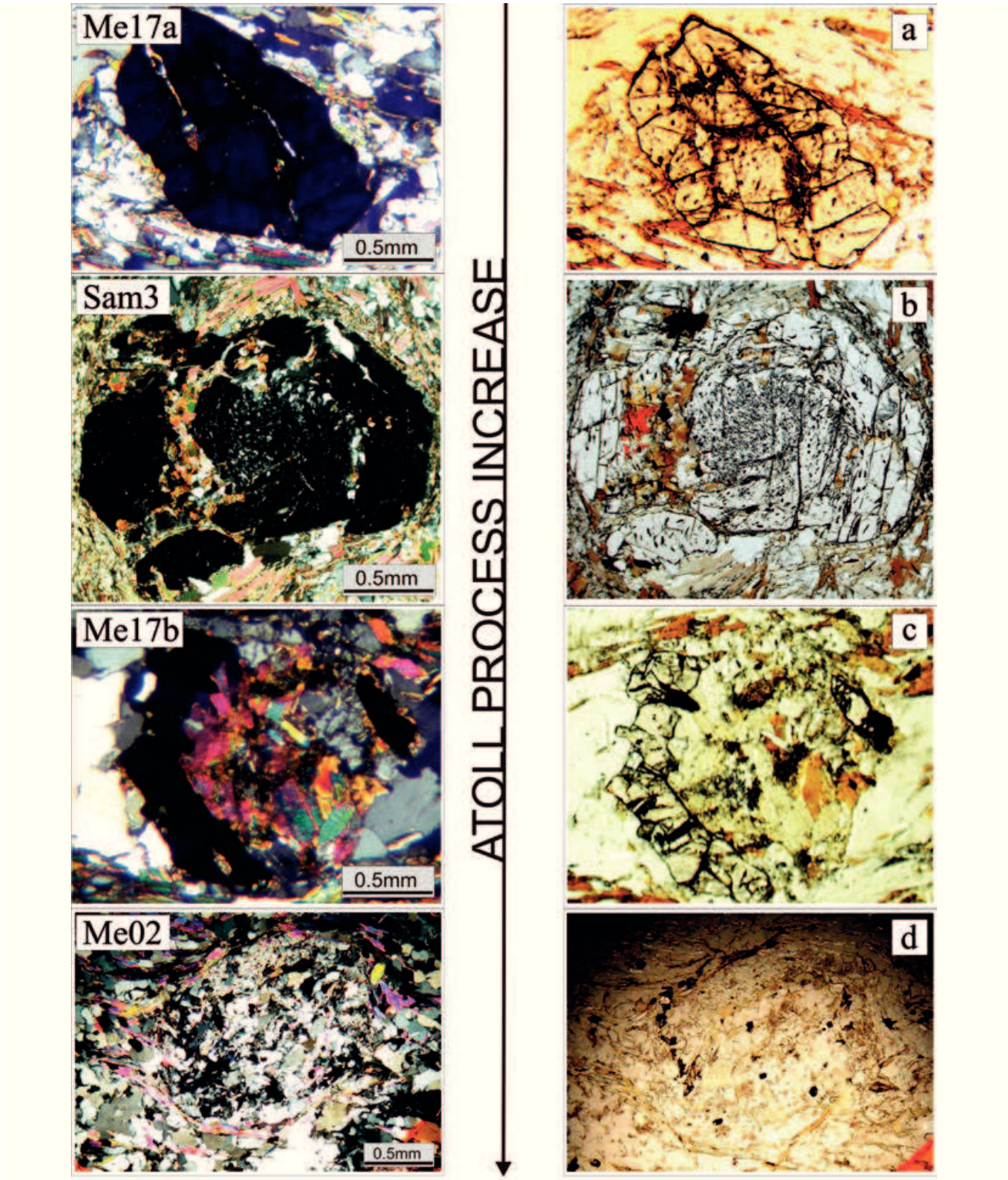

Figure 6. Microphotographs of sequential steps of atoll garnet formation, with atoll process increasing from a to d (crossed and parallel polarizers, respectively). a) "Pristine" fractured garnet; b) Preserved garnet core, relict outer core is partially transformed to biotite, muscovite, plagioclase, quartz aggregate; outer rim is preserved; c) typical atoll texture where a rim of garnet surrounds a white mica, biotite, chlorite, plagioclase and quartz aggregate; d) garnet completely pseudomorphed by white mica, biotite, chlorite, plagioclase and quartz aggregate.

completely pseudomorphed (Figure 6d).

The first step of atoll textural evolution, is characterized by the presence of a complete garnet, which is wrapped by S2 foliation and preserves an inclusion-rich (ilmenite, white mica, chloritized biotite apatite) core, rimmed by an inclusion-poor outer core and rim (Figure 6a).

The second step of atoll textural evolution (Figure 6b) is represented by a garnet with a partly resorbed core, characterized by the presence of sigma shaped inclusion trails, testifying the syn-D1 growth event followed by the progressive crenulation of the former schistosity (S1) in non-coaxial regime until the formation of the main schistosity (S2) (Robyr et al., 2007). The recognition of an outer euhedral inclusion-poor mantle likely indicates a later D1 quasi-static porphyroblast growth. The crystallization of Bt, Pl, Wm and Chl localized along fractures is correlated with a retrograde metamorphic event (D2).

The third step of atoll textural evolution (Figure 6c) represents the most advanced state of atollization. Here garnet cores are totally replaced by plagioclase, quartz, biotite, and white mica in contact with inclusion-free garnet ring. The crystallographic orientation of biotite and white mica, seems to be controlled by the formation of 111 garnet planes in the inner part of the ring, while they are randomly-oriented, compared to the main external foliation (Figure 5b).

The last stage of atollization is represented in the fourth selected micro-domain characterized by the total substitution of garnet by an assemblage of white mica, biotite, chlorite, plagioclase and quartz (Figure 6d).

Image analysis and mineral-chemical evolution

BSE images and X-ray map arrays of the four sequential steps of atoll shaped garnet formation were here integrated with the multivariate statistical analysis undertaken with the software X-Ray Map Analyzer (Ortolano et al., 2014), in order to define the sequence of garnet zones with different compositions linked to the recognized metamorphic evolution.

BSE images of the complete garnet (Figure 7A) evidence the presence of inclusions preferentially concentrated into the inner garnet portion and decreasing towards the rim. X-ray maps highlight a typical bell shaped profile, interrupted by an anomalous increase of Mn concentration which is especially evident along the fractures that connect the inner garnet portion with the external matrix minerals (Figure 7B - ME17a). The result of the first analytical cycle evidences the distribution and the nature of the inclusions mostly constituted by ilmenite (1.02%), biotite (0.97%), quartz (0.73%) and white mica (0.58%) and minor phases (Figure 7C - ME17a - Appendix C). The late-D1 overgrowing stage is also well defined by sub-euhedral garnet with few or no inclusions, which account in total for the 97.18%, considering as 100% the portion of the rim domain (Appendix C).

BSE image of the second microdomain evidenced the presence of a peninsula constituted by an inclusion-rich garnet, bracketed in part by plagioclase and biotite and by the overgrowth of the late-D1 inclusion-poor garnet (Figure 7A -

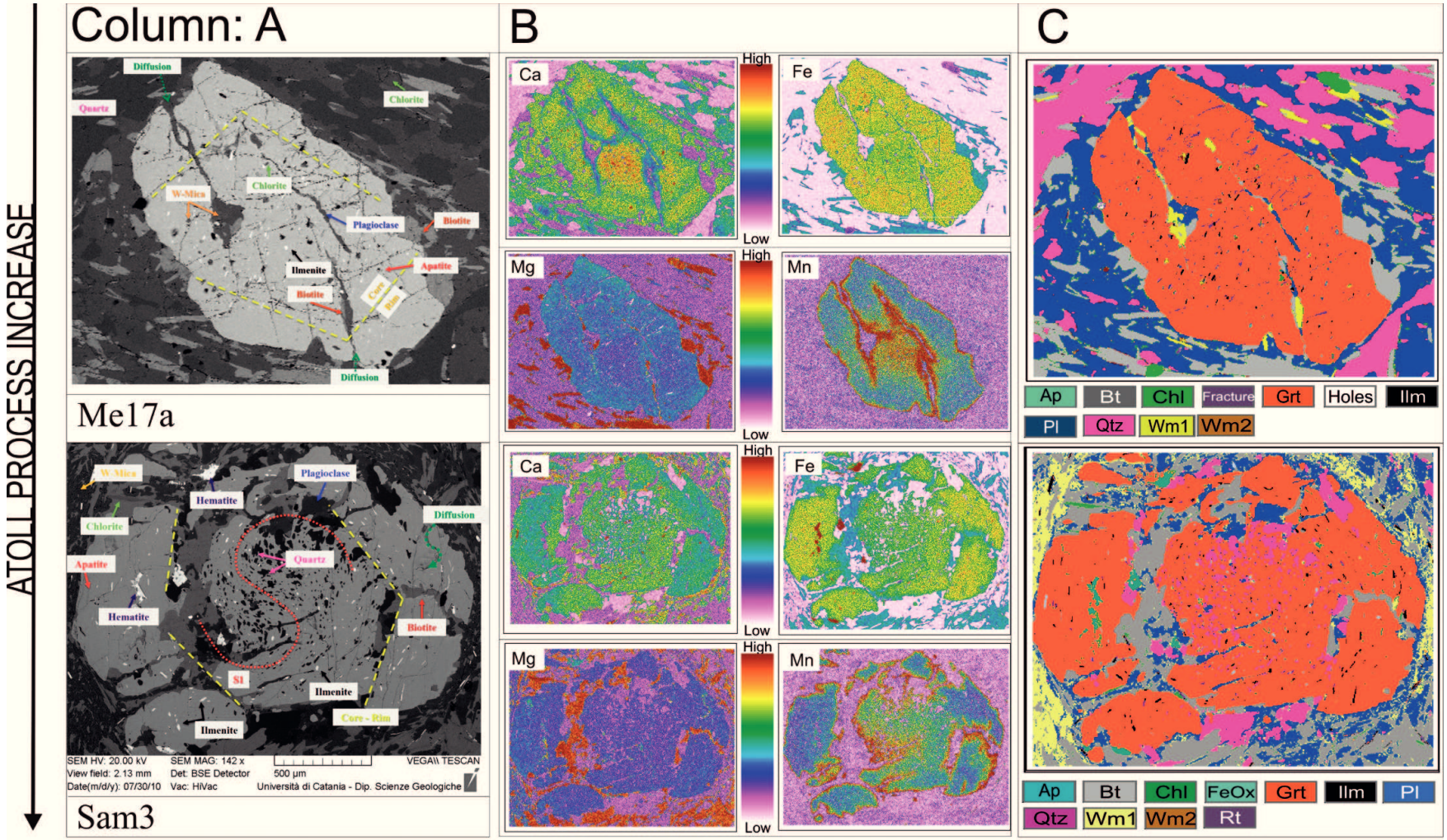

Figure 7. Back scattered electron images (column A); X-ray maps (column B); first cycle image classification results (column C) for the first two sequential atollization steps.

SAM3). X-ray maps evidence that the original bell-shaped profile of Mn is here almost completely obliterated by the formation of a new garnet richer in Mn than the core. This suggests that, in this case, the fluids derived from the partial resorption of the relic inner core were enriched in Mn during the atoll-forming retrograde reactions due to the enrichment of this element in the core (Figure 7B - SAM3). The above features are in agreement with the results of the first analytical cycle, which recognizes the presence in the garnet core of a sigma shaped inclusions, constituted by qtz - pl - ilm - wm - bt - ap (Figure 7C - SAM3 - Appendix C), overgrown by the late-D1 garnet formation.

In the third micro-domain, representative of the total garnet inner core pseudomorphosys, BSE image has evidenced the textural relations between the phases replacing the core (mostly plagioclase and white mica) and the inner rim at the contact (Figure 8A - ME17b). X ray maps evidence a peculiar zoning pattern of the garnet ring, characterized by an increasing content of Mn especially along the fractures as well as in the inner rim portion of the ring (Figure 8B - ME17b). The first analytical cycle has highlighted the presence of biotite in contact with neoblastic garnet (grt3) with rational sharp boundaries associated to plagioclase and small muscovite flakes (wm 3) (Figure 8C - ME17b). The BSE image of the last selected domain, representative of the total pseudomorphosys, evidences the presence of a qtz - pl - bt - sph - wm - chl aggregate that completely substitutes garnet, whose presence is here suggested only by its shape as it is completely pseudomorphed (Figure 8A - ME02). X ray maps seem to delineate (especially in the Ca-Fe-Mg channels) the old inclusion trails within the core, whereas the Si channel allow to emphasize the presence of plagioclase clearly depicted the original garnet boundary (Figure 8B - ME02). This last evidence have been then confirmed by the output of the first analytical cycle which delineates the boundary of the preexisting garnet through the shape of the plagioclase in the upper right portion of the map, characterized by an alignment along the 111 planes of the previously existing garnet (Figure 8C - ME02).

The second analytical cycle consists in the chemical sub-classification as well as in the computation of the kernel density distribution of an element within a selected phase (Ortolano et al., 2014). Results on the garnets of the first three domains, allow to define the peculiar compositional zoning pattern, which includes up to four distinct regions related to different atoll garnet formation stages, permitting at the same time to interpret the results of the mineral-chemical analysis. In this view, a new set of acronyms are proposed in order to outline the evolutionary stages of the atolls formation even though they are not always observed at the same time in all the selected microdomains: i) RIC (*Relic Inner Core*); ii) ROC (*Relic Outer Core*); iii) RR (*Relic Rim*) and iv) NR (*New Rim*) (Table 3).

The RIC zone, recognized in the garnets of samples Me17 and Sam3 is characterized by low contents in almandine and pyrope and high content in spessartine and grossular (Figure 9 a,b) ranging from $Alm_{59}Grs_{24}Pyr_{6}Sps_{11}$ to

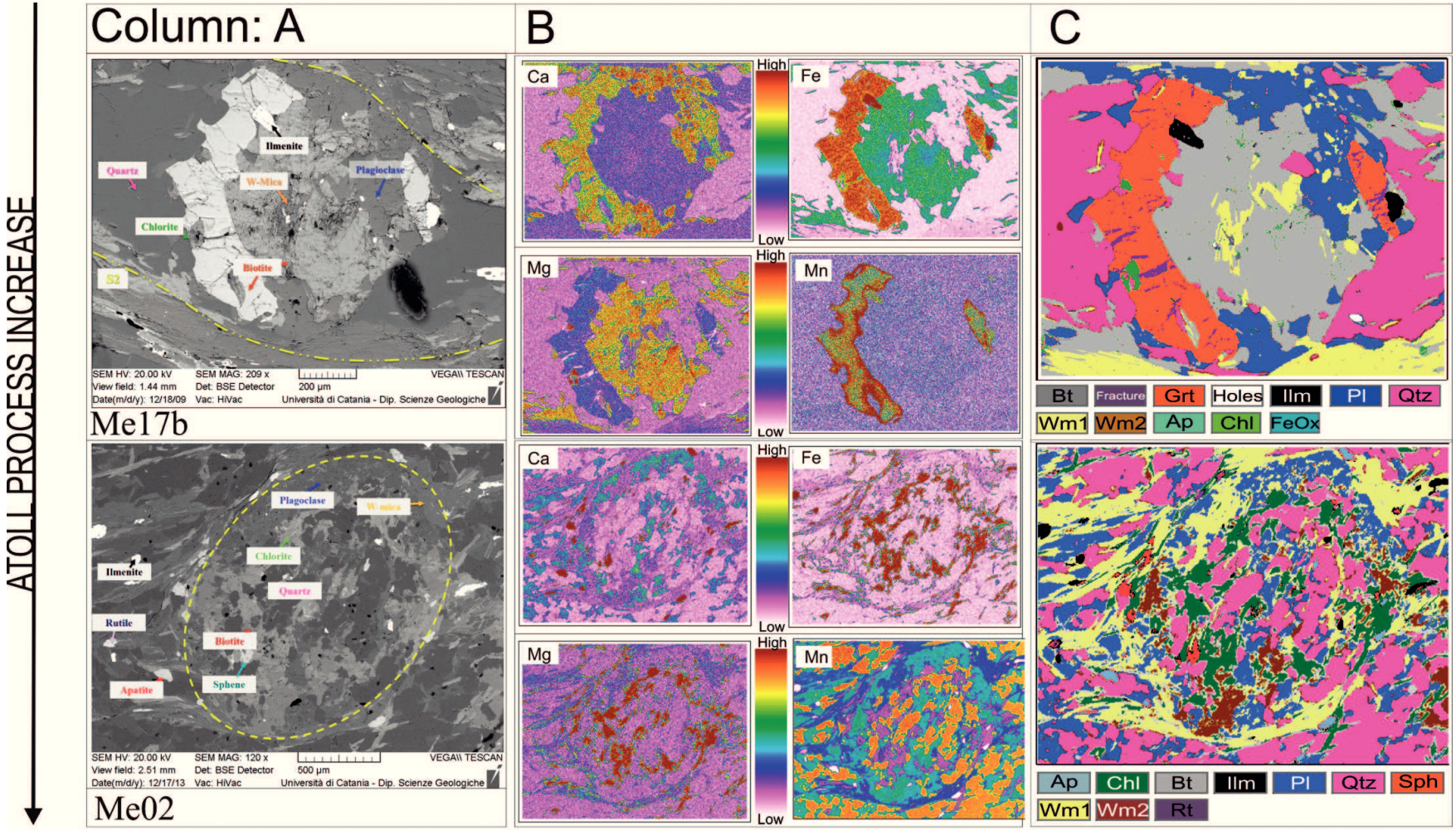

Figure 8. Back scattered electron images (column A); X-ray maps (column B); first cycle image classification results (column C) for the last two sequential atollization steps.

Table 3. Subdivision of garnet zones after the XRMA 2nd analytical cycle.

Image analysis zones		Mineralogical phases	Sample	Composition	Inclusions	Deformation stage
RIC	Relic Inner Core	Grt 1	Me17; Sam3	(Alm59Grs24Pyr6Sps11) to (Alm63Grs18Pyr6Sps13)	Ilm + Qtz + Wm ± Chl	Sin-S1
ROC	Relic Outer Core	Grt 2	Me17; Sam3	(Alm65Grs15Pyr11Sps9) to (Alm69Grs17Pyr10Sps4)	Ilm + Qtz + Wm + Bt + Ap	Late-S1
RR	Relic Rim		Sam3	(Alm66Grs16Pyr9Sps9) to (Alm70Grs15Pyr11Sps4)	Ilm + Ap + Hem	
NR	New Rim	Grt 3	Me17; Sam3	(Alm63Grs15Pyr8Sps14) to (Alm67Grs6Pyr10Sps17)	Qtz + Ap + Bt + Pl	Sin-S2

$Alm_{63}Grs_{18}Pyr_6Sps_{13}$ (Figure 10 - Appendix D). The ROC zone was observed in all selected domains and is characterized by a decrease in spessartine and a simultaneous increase in almandine and, to a lesser extent, in pyrope (Figure 9 a,b,c). Compositions vary from $Alm_{65}Grs_{15}Pyr_{11}Sps_9$ to $Alm_{69}Grs_{17}Pyr_{10}Sps_4$ along the outer edge, exhibiting a gradual reduction of spessartine from the inner core to the garnet rim and by the decrease in grossular (Figure 10 - Appendix D). The RR zone ($Alm_{68}Grs_{16}Pyr_8Sps_8$ to $Alm_{70}Grs_{15}Pyr_{11}Sps_4$) (Figure 10 - Appendix D) has been recognized only in sample Sam3 (Figure 9b). It is characterized by a sharp discontinuity defined by a steep increase in almandine and pyrope associated with a decrease in grossular and spessartine, clearly visible in the compositional profiles of Figure 10. In all analyzed domains a NR zone, localized along fractures ($Alm_{63}Grs_{15}Pyr_8Sps_{14}$) and along the outer margins ($Alm_{67}Grs_6Pyr_{10}Sps_{17}$), has been observed (Appendix D). This zone is characterized by a sharp increase in spessartine content, suggesting that a garnet core consuming reaction took place (Figure 9 a,b,c), and that the Mn held in the core was incorporated in the new garnet rims. (i.e the reaction grt1+ included minerals + fluids(?) = grt3 + wm + bt + pl + qtz).

The growth sequence is clearly visible in Figure 10 as well as in Appendix D, where the garnet composition from RIC to RR is characterized by an increase in Grs and Alm, whereas the NR garnet composition is noticeably Spess rich. This evidence can be explained through the selective resorption of the original garnet cores composition which allowed to enrich the retrograde reaction fluid with Mn. The

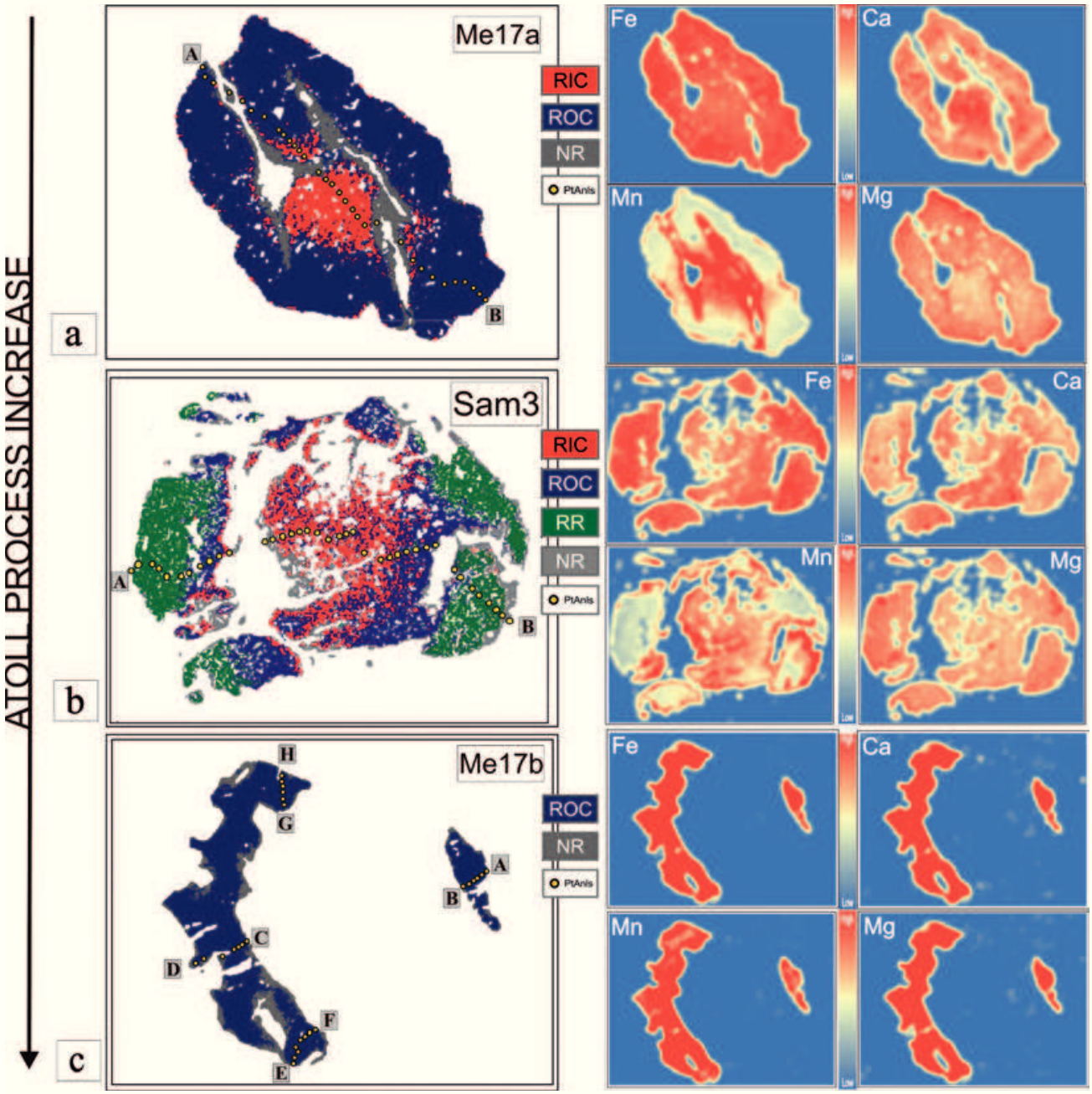

Figure 9. Second cycle of the image classification results for the three garnet characterized by an increasing stage of atollization (RIC = Relic Inner Core, ROC = Relic Outer Core, RR = Relic Rim and NR = New Rim): a) Outputs relative to the first microdomain of the Me17 sample; b) Outputs relative to the microdomains of the Sam3 sample; c) Outputs relative to the second microdomain of the Me17 sample.

new garnet (i.e. NR) forms from the reaction of old inner cores garnet connected by fractures with matrix minerals.

White mica occurs both in the matrix, aligned parallel to the S2 foliation, and inside the atoll structure, as a replacement phase. It is a muscovite with Si ranging from 3.09 to 3.17 a.p.f.u, with a low to intermediate phengite content (Appendix

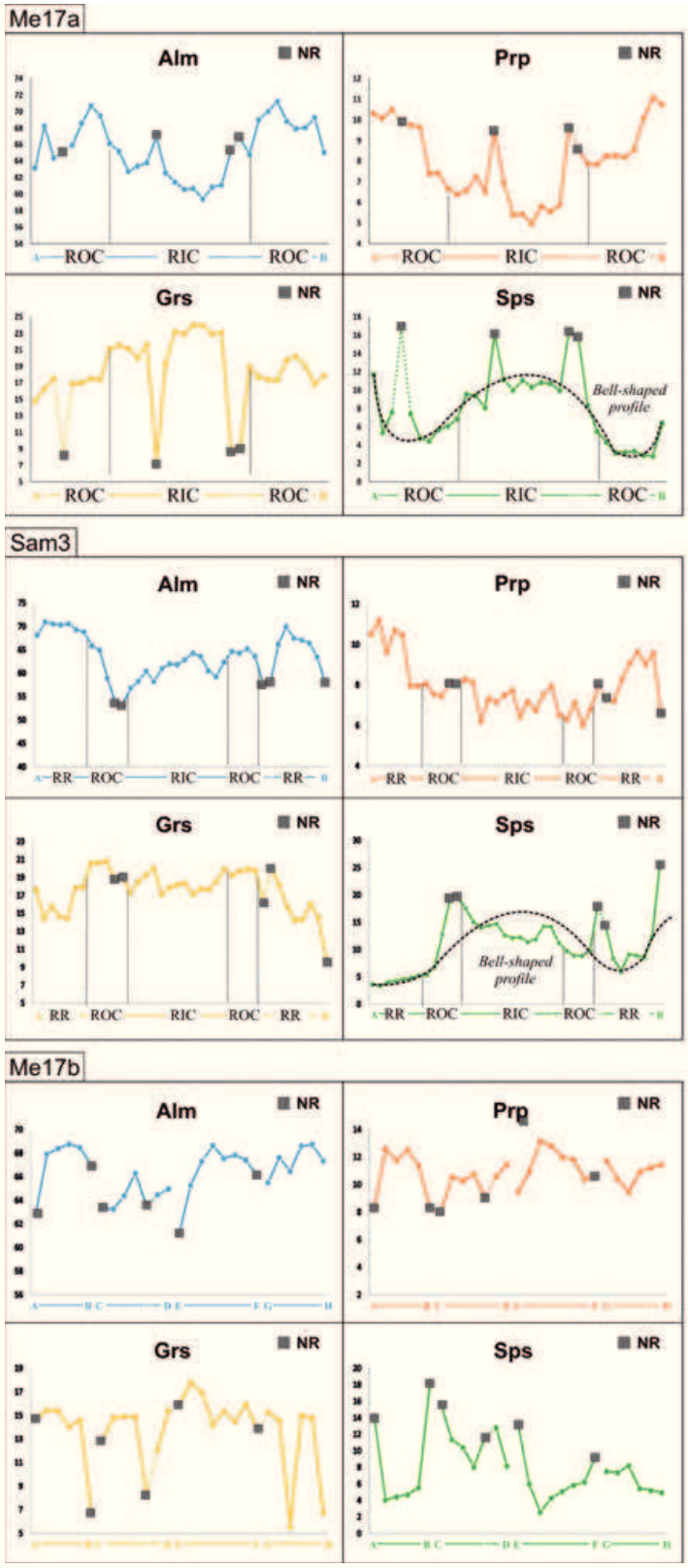

Figure 10. Compositional profiles of the three garnet characterized by the increasing stage of atollization process relative to the first microdomain of Me17, Sam3 and the second microdomain of the Me17 samples (for spot analysis location see yellow dots on Figure 9).

A). Muscovite with low Si content is observed inside the atoll, whereas syn-S2 muscovite is more phengite-rich.

Plagioclase is found either as a replacement in the atoll core, or as a granoblastic phase in the matrix (syn-S2). It has andesine composition (from An_{32} to An_{37}) in the atolls, whereas it has higher An content (from An_{37} to An_{50}, Appendix A) in the matrix.

Biotite has XFe (= Fe/Fe + Mg) ranging from 0.27 to 0.55 inside the atoll, whereas the syn-S2 crystals show a smaller range (XFe from 0.44 to 0.48) in the matrix.

Chlorite compositions (pseodomorphs after biotite and subordinately after garnet) are characterized by XFe from 0.37 to 0.51, typical of pycnochlorite.

Ilmenite has a relatively significant pyrophanite content (Mn-ilmenite) ranging from 9.4 to 10.7 mol% in the atolls, whereas a wider range (from 2.8 to 15.1 mol%) can be detected in the matrix, (Appendix B).

Thermodynamic modeling and PT pseudosection computation

Two pseudosections were calculated for samples SAM3 and ME17 using the Perple_X software package (updated to March 2014, http://www.perplex.ethz.ch/). XRF compositions were chosen to represent the effective bulk rock chemistry. In both cases the pseudosections encompass a relatively restricted PT range of T = 500-650 °C and P = 0.3-1.1 GPa, considered sufficient to bracket the PT constraints of the observed parageneses. MnO-Na_2O-K_2O-FeO-MgO-Al_2O_3-SiO_2-H_2O (MnNKFMASH) system was used. SiO_2 and H_2O were considered in excess and the CORK fluid equation of state (EOS) of Holland and Powell (1998) was used to model the fluid phase behavior. The solid solution models were: (a) Ti-Fe^{3+} biotite of Tajcmanova et al., (2009) extended for Mn solution after Tinkham et al., (2001); (b) a quaternary garnet model of Holland and Powell (1998); (c) the white mica model of Holland and Powell (1998) valid for Na-poor compositions; (d) the chlorite model of Holland et al., (1998); (e) a binary plagioclase solid solution (Newton et al., 1980). According to Evans (2004) and Cirrincione et al. (2008), in order to derive reliable P-T constraints, the intersections of at least three isopleths per time were considered from the different garnet compositions texturally constrained by means of the image processing. As the specific garnet compositional range is in equilibrium with the bulk-rock chemistry, it is possible to calculate the P-T conditions of the different garnet growth stages within an average estimated error of ± 30 °C and ± 0.1 GPa (e.g. Cirrincione et al., 2008), assuming that small volumes have preserved the equilibrium assemblages and compositions.

The Me17 garnet isopleths intersections in RIC ($Alm_{59\text{-}63}Grs_{18\text{-}24}Prp_{5\text{-}6}Sps_{11\text{-}13}$) define a PT interval of T = 545-560 °C and P = 0.68-0.72 GPa, whereas those of ROC ($Alm_{65\text{-}69}Grs_{15\text{-}17}Prp_{10\text{-}14}Sps_{4\text{-}9}$) define a slightly larger area with T = 567-590 °C and P = 0.72-0.83 GPa (Figure 11 a,b).

The Sam3 garnet isopleths intersections related to RIC ($Alm_{58\text{-}62}Grs_{17\text{-}20}Prp_{7\text{-}9}Sps_{12\text{-}15}$) delimit an area enclosed between T = 555-565

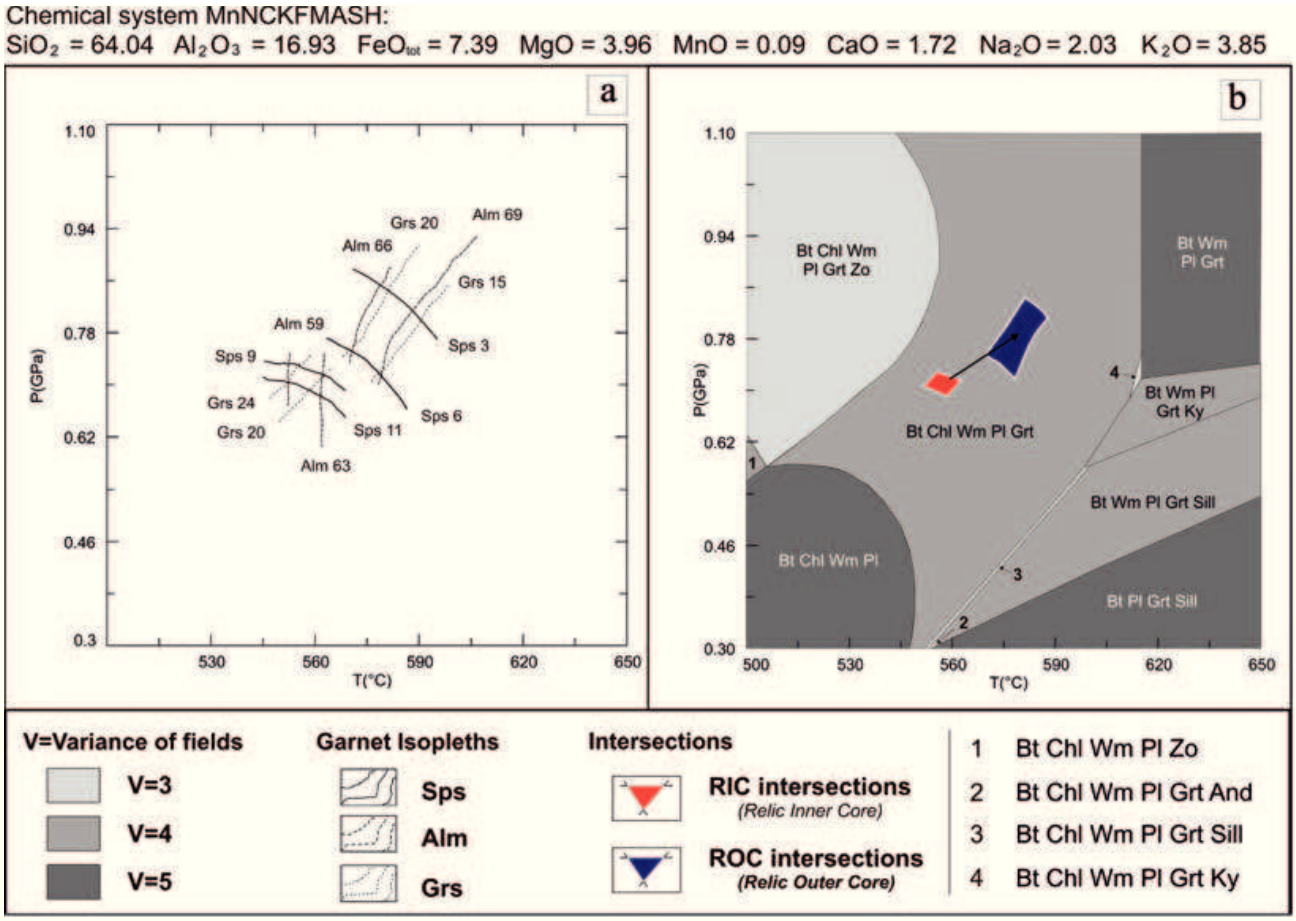

Figure 11. Pseudosections calculated for Me17 with effective bulk rock chemistry derived from XRF. a) Isopleths intersections for garnet composition in sample Me17; b) pseudosection of sample Me17 with light areas evidencing isopleths intersections for RIC (red) and ROC (dark blue).

°C and P = 0.59-0.63 GPa, whereas the ROC ($Alm_{64-65}Grs_{18-19}Prp_{10-11}Sps_{6-8}$) defines a range of T = 580-585 °C and P = 0.68-0.72 GPa. The RR ($Alm_{65-67}Grs_{14-17}Prp_{8-11}Sps_{6-9}$) falling in an area corresponding to lower pressures and higher temperatures compared with the ROC, and it is between T = 590-600 °C and P = 0.58-0.66 GPa (Figure 12 a,b).

In order to estimate the P-T conditions associated with the retrograde metamorphic evolution responsible for the breakdown of the garnet inner core and for the consequent NR formation, a representative portion of the relative equilibrium volume from Me17 and Me02 samples has been used to calculate a new effective bulk rock chemistry, isolating, by means of ArcGis raster analysis (Dainelli et al., 2010), the portion of the aggregate substituting the core + grt3 (Figure 13). Once the modal amount of the new phases and their composition was known (Tables 4a and 5a), the bulk composition of this volume can be determined (Tables 4b and 5b).

The new computed pseudosection for Me17

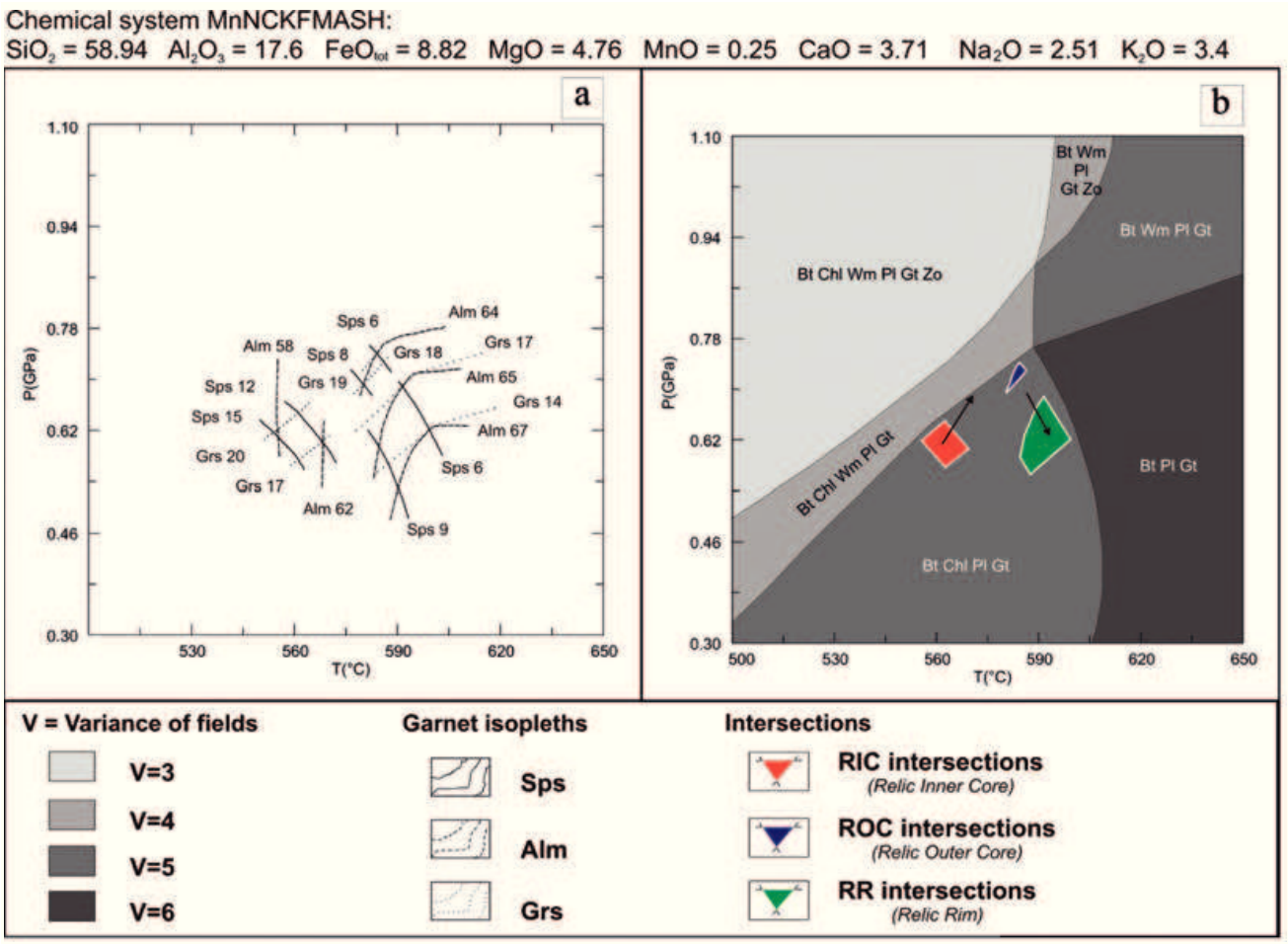

Figure 12. Pseudosections calculated for Sam3 with effective bulk rock composition derived from XRF. a) Isopleths for garnet composition in sample Sam3; b) pseudosection of sample Sam3 with light areas evidencing isopleths intersections for RIC (red), ROC (dark) and RR (green). See text for explanation of abbreviations and textures.

(former garnet core) was calculated, assuming the effective bulk rock chemistry from Table 4b in the (MnNKFMASH) system, using the same solid solution models and EOS as before. NR garnet isopleth intersection ($Alm_{61-67}Grs_{8-12}Prp_{0-23}Sps_{8-19}$) in equilibrium with anorthite (An_{31-35}) and phengite (Ph_{8-12}), in association with an average XFe biotite of 47%, delimit an area characterized by temperatures ranging from 563 to 600 °C and by pressures from 0.48 to 0.70 GPa, which falls at a higher temperature and lower pressure with respect to the previously constrained P-T conditions for D1 (Figure 14 a,b).

Effective bulk rock chemistry for Me02 (Table 5b), representative for the total garnet pseudomorphosis, was used to calculate a new pseudosection in the NaKFMASH system, with the same EOS and solid solutions, and adding Fe-Mg-Mn staurolite ideal model after Holland and Powell (1998) because stable in some fields of the right portion of the new computed pseudosection. The plagioclase (An_{13-15}),

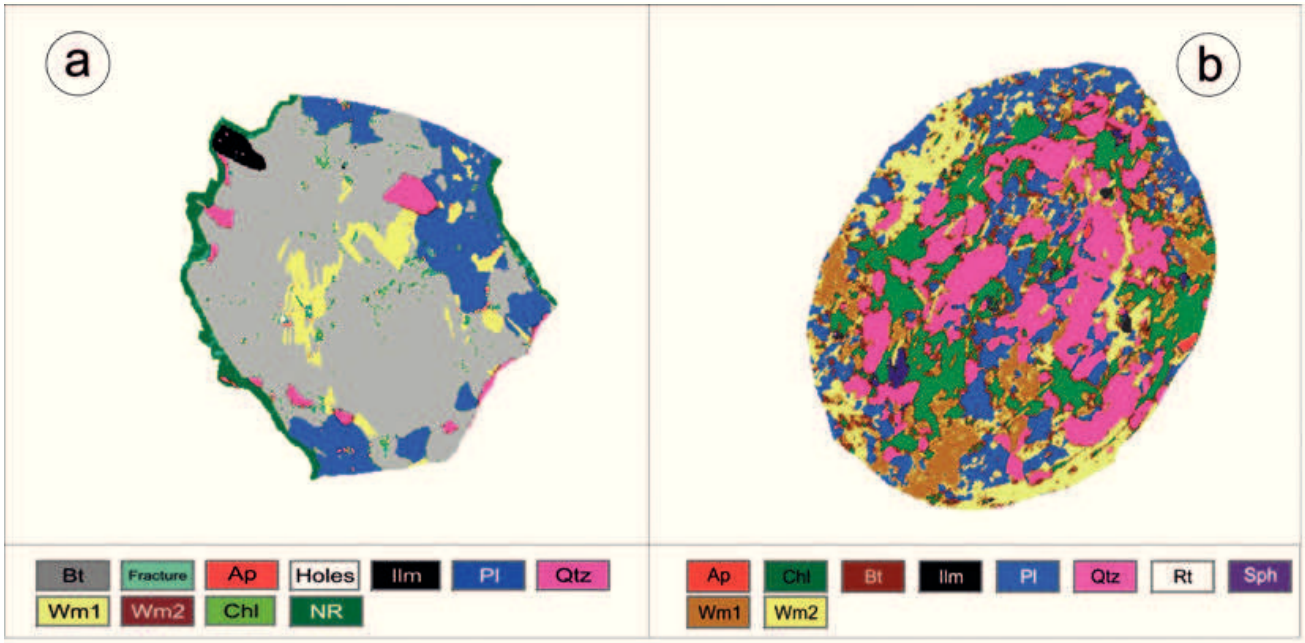

Figure 13. Image resulting from the combination of the two cycles of image analysis for atoll garnet Me17 (a) and for pseudomorphed garnet in sample Me02 (b). The areas occupied by garnets are evidenced in order to determine the equilibrium volume that reacted during the D2 event. Obtained effective bulk rock chemistry was then used to calculate the retrograde pseudosections of Figure 14.

Table 4a. Quantitative output data of the supervised image classification from Me17b selected domain and from isolated retrograde reactant portion.

Quantitative data of Me17 total domain			Quantitative data of Me17 isolated polygon		Mineral phases polygon/domain
Mineral	Pixel count	Percentage	Pixel count	Percentage	Percentage
NR	28203	13.77	3834	5.57	1.87
Qtz	51318	25.06	1782	2.59	0.87
Pl	33239	16.23	11704	16.99	5.71
Bt	62774	30.65	43672	63.40	21.32
Wm1	19089	9.32	4801	6.97	2.34
Chl	2159	1.05	830	1.20	0.41
Ilm	1597	0.78	870	1.26	0.42
Ap	564	0.28	279	0.41	0.14
Holes	177	0.09	50	0.07	0.02
Fracture	2943	1.44	713	1.04	0.35
FeOx	28	0.01	4	0.01	0.00
Wm2	2709	1.32	343	0.50	0.17
Total	204800	100.00	68882	100.00	33.63

Table 4b. Oxides modal amount computation inside mineral phases of the isolated polygon (Me17b).

Garnet oxides computation											
Oxides	SiO_2	TiO_2	Al_2O_3	Cr_2O_3	FeO	MnO	MgO	CaO	Na_2O	K_2O	Total
Average composition (wt%)	38.11	0.13	21.47	0.14	27.48	5.89	2.12	4.28	0.00	0.00	99.61
Normalized to 100	38.26	0.13	21.55	0.14	27.59	5.91	2.12	4.29	0.00	0.00	100.00
Garnet polygon oxides	0.72	0.00	0.40	0.00	0.52	0.11	0.04	0.08	0.00	0.00	1.87
Feldspar oxides computation											
Average composition (wt%)	62.17	0.00	24.45	0.00	0.00	0.00	0.00	5.09	7.67	0.00	99.38
Normalized to 100	38.26	0.13	21.55	0.14	27.59	5.91	2.12	4.29	0.00	0.00	100.00
Feldspar polygon oxides	0.72	0.00	0.40	0.00	0.52	0.11	0.04	0.08	0.00	0.00	1.87
Biotite amount compuation											
Average composition (wt%)	37.91	1.45	20.08	0.00	15.91	0.21	11.52	0.00	0.37	8.50	95.94
Normalized to 100	39.52	1.51	20.93	0.00	16.58	0.21	12.00	0.00	0.38	8.86	100.00
Biotite polygon oxides	8.43	0.32	4.46	0.00	3.54	0.05	2.56	0.00	0.08	1.89	21.32
White mica oxides computation											
Average composition (wt%)	47.39	0.63	36.11	0.00	0.88	0.00	0.69	0.00	1.22	9.03	95.95
Normalized to 100	49.39	0.66	37.63	0.00	0.92	0.00	0.72	0.00	1.27	9.41	100.00
Wm polygon oxides	1.24	0.02	0.94	0.00	0.02	0.00	0.02	0.00	0.03	0.24	2.51
Chlorite oxides computation											
Average composition (wt%)	29.32	0.00	20.55	0.00	22.50	0.00	15.93	0.00	0.00	0.00	88.30
Normalized to 100	33.20	0.00	23.27	0.00	25.48	0.00	18.04	0.00	0.00	0.00	100.00
Chl polygon oxides	0.14	0.00	0.10	0.00	0.10	0.00	0.07	0.00	0.00	0.00	0.41
Sum of the oxides to detect new effectively bulk chemistry for isolated D2-polygon											
Oxides	SiO_2	TiO_2	Al_2O_3	Cr_2O_3	FeO	MnO	MgO	CaO	Na_2O	K_2O	Total
Domain Oxides	14.82	0.34	7.31	0.00	4.18	0.16	2.69	0.37	0.55	2.13	32.55
Normalized to 100	45.53	1.05	22.46	0.00	12.84	0.48	8.27	1.15	1.70	6.53	100.00
Normalized to 100 (- TiO_2) in order to obtain new bulk chemistry	46.01	0.00	22.69	0.00	12.98	0.49	8.36	1.16	1.72	6.60	100.00

phengite (Ph_{6-9}) and XFe average value for chlorite of 46%, permitted to obtain isopleths intersections delimiting a relatively wide portion of the PT space between T = 500-600 °C and P = 0.46-0.70 GPa, suggesting a retrograde evolution towards greenschist facies conditions (Figure 15 a,b).

Discussion

Thermodynamic modeling via PT pseudosection computation constrained by means of textural relationships of four micro-domains from micaschist belonging to the Aspromonte Peloritani Unit, were here performed in order to reconstruct the PT evolution of the rocks involved in the Variscan

Tale 5a. Quantitative output data of the supervised image classification from Me02 selected domain and from isolated reacted portions.

Quantitative data of Me02 total domain			Quantitative data of Me02 isolated polygon		Mineral phases polygon/domain
Mineral	Pixel count	Percentage	Pixel count	Percentage	Percentage
Qtz	59067	28.84	19058	21.71	9.31
Pl	37823	18.47	15993	18.22	7.81
Chl	21825	10.66	14930	17.00	7.29
Bt	24383	11.91	12143	13.83	5.93
Wm1	15343	7.49	9002	10.25	4.40
Wm2	40959	20.00	15103	17.20	7.37
Ap	976	0.48	227	0.26	0.11
Rt	153	0.07	8	0.01	0.00
Ilm	2251	1.10	661	0.75	0.32
Sph	1677	0.82	614	0.70	0.30
FeOx	343	0.17	60	0.07	0.03
Total	204800	100.00	68882	100.00	33.63

Table 5b. Oxides modal amount computation inside mineral phases of the isolated polygon.

Feldspar oxides calculation										
Oxides	SiO_2	TiO_2	Al_2O_3	FeO	MnO	MgO	CaO	Na_2O	K_2O	Total
Average composition (wt%)	63.75	0.00	22.73	0.00	0.00	0.02	3.92	8.83	0.00	99.25
Normalized to 100	64.23	0.00	22.90	0.00	0.00	0.02	3.95	8.90	0.00	100.00
Feldspar polygon oxides	5.02	0.00	1.79	0.00	0.00	0.00	0.31	0.69	0.00	7.81
White mica oxides calculation										
Average composition (wt%)	47.03	0.74	34.56	2.09	0.00	1.24	0.00	0.85	9.36	95.87
Normalized to 100	49.06	0.77	36.05	2.18	0.00	1.29	0.00	0.89	9.76	100.00
Wm polygon oxides	3.81	0.06	2.80	0.17	0.00	0.10	0.00	0.07	0.76	7.77
Chlorite oxides calculation										
Average composition (wt%)	28.64	0.00	20.91	23.13	0.00	15.86	0.00	0.00	0.08	88.62
Normalized to 100	32.32	0.00	23.60	26.10	0.00	17.89	0.00	0.00	0.09	100.00
Chl polygon oxides	2.36	0.00	1.72	1.90	0.00	1.30	0.00	0.00	0.01	7.29
Biotite oxides calculation										
Average composition (wt%)	28.64	0.00	20.91	23.13	0.00	15.86	0.00	0.00	0.08	88.62
Normalized to 100	32.32	0.00	23.60	26.10	0.00	17.89	0.00	0.00	0.09	100.00
Bt polygon oxides	2.36	0.00	1.72	1.90	0.00	1.30	0.00	0.00	0.01	7.29
Sum of the oxides to detect new effectively bulck chemistry for isolated D2-polygon										
Domain Oxides	22.49	0.06	6.39	2.20	0.00	1.49	0.29	0.73	0.78	34.44
Normalized to 100	65.31	0.18	18.57	6.38	0.00	4.33	0.85	2.12	2.28	100.00
Normalized to 100 (- TiO_2) in order to obtain new bulk chemistry	65.42		18.60	6.39	0.00	4.34	0.85	2.12	2.28	100.00

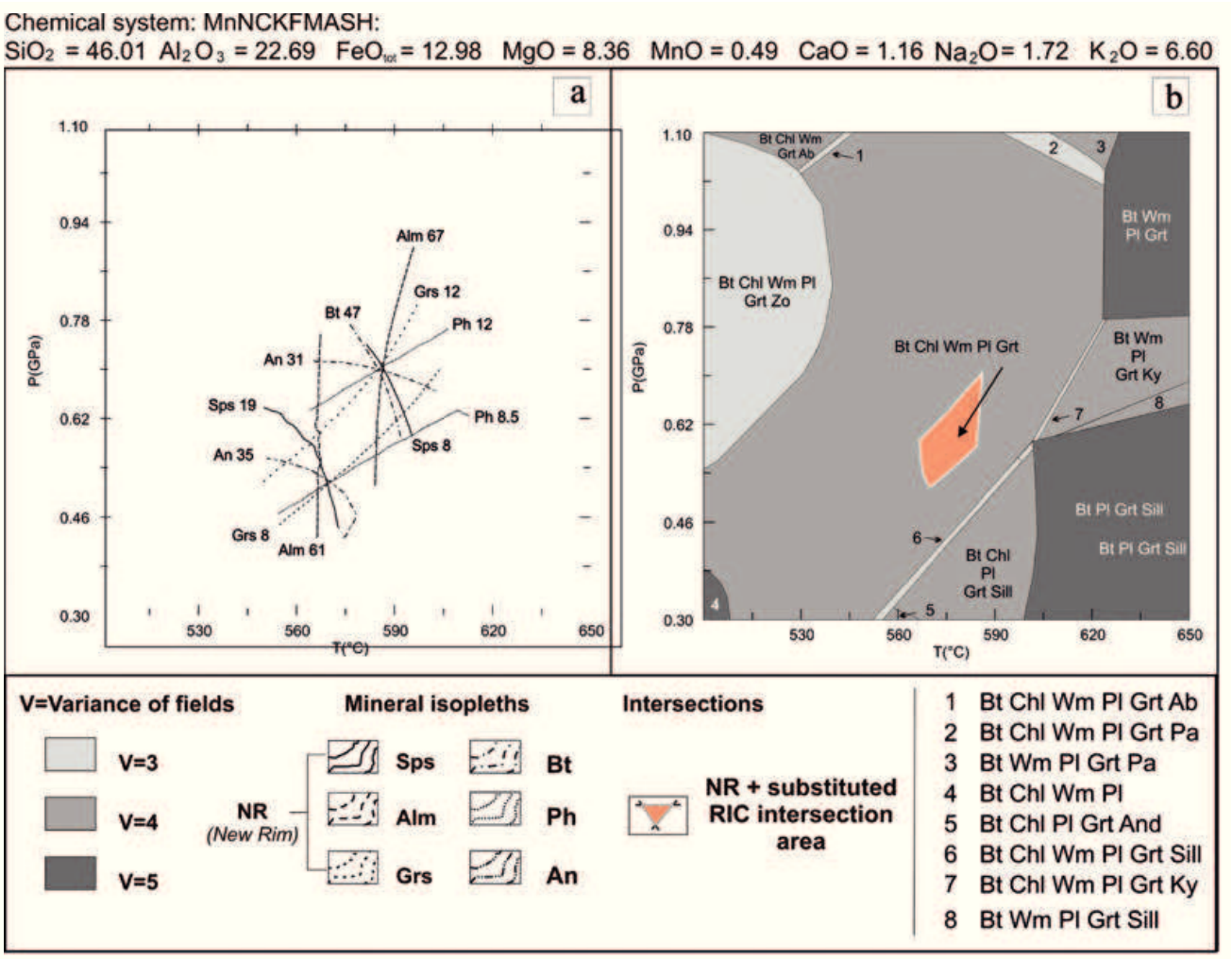

Figure 14. Pseudosections calculated for Me17 using bulk composition determined after evaluation of the volume that reacted during the D2 event (Table 4b). a) Isopleths for garnet composition in sample Me17; b) pseudosection of sample Me17 with light areas evidencing isopleths intersections for aggregates substituting garnet cores.

orogeny. With the support of a multivariate statistical image analysis of X-Ray maps, this approach also allowed to reconstruct the progressive steps of atoll garnet formation during the retrograde PT evolution: Atoll garnet formation can be here related to the substitution of garnet cores during the D2 stage, with the consumption of garnet cores (grt1) and production of a third generation of garnet (grt3). Garnet 3 is in fact concentrated along fractures or as thin rims around the relic garnet ring in advanced state of atollization. Grt3 resulted clearly in textural equilibrium with wm3, bi3, qtz and pl3, well preserved within the atoll as a result of the reaction between the previously formed inclusion-rich garnet inner-core (grt1), interacting with matrix minerals via fluid flow through fractures linking the innermost part of the garnet with the matrix itself.

The petrographic investigations evidence the

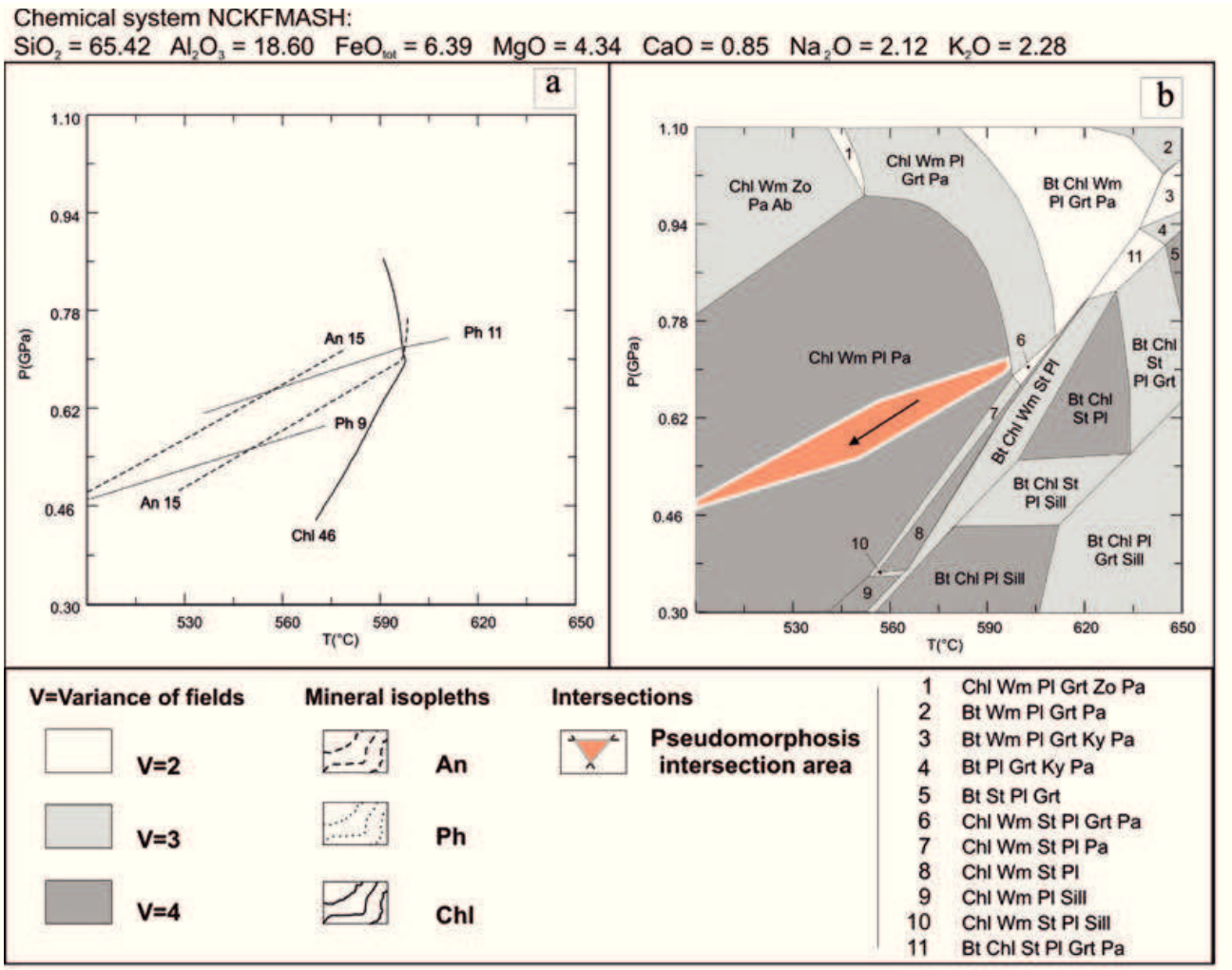

Figure 15. Pseudosections calculated for Me02 using bulk composition determined after evaluation of the volume that reacted during the D2 event (Table 5b): a) Isopleths for garnet composition in sample Me02; b) pseudosection of sample Me02 with light areas evidencing isopleths intersections for aggregates substituting garnet cores.

presence of three different garnet generations. The recognition of the stages of garnet growth and the definition of the associated parageneses has been obtained using image analysis coupled with compositional maps, performed with a dedicated software (Ortolano et al., 2014). This approach allowed: (a) to couple textural observation at the microscope, with textural observations obtained from compositional maps and; (b) to individuate a series of garnets that exemplify different steps of the atoll formation: from garnets preserving intact zonings, to garnets that are partially substituted, to garnets that show a completely developed atoll texture. Each of these steps is characterized by peculiar and specific garnet compositions. The observed changes of mineral phases compositions during the progressive steps of the development of the atoll texture and the successive deformation episodes determining recrystallization of the

rocks, allowed the reconstruction of the metamorphic history registered by the samples, as well as. the recognition of the mechanisms of formation of atoll structures.

PT conditions associated to the three recrystallization phases have been determined from pseudosections. Equilibrium volumes during the different stages of the metamorphic evolution were determined using XRF bulk compositions for the early garnet growth stages and by modal analysis via image analysis, for the late atoll shaped garnet formation.

As a matter of fact, the bulk rock composition approximates reasonably the equilibrium volume of the first stages of recrystallization, permitting to predict the assemblages associated to S1 and S2. In order to determine the composition representing the equilibrium volume during garnet core consumption, it was necessary to calculate the volume representing the part of the thin section that reacted during this stage, comparing it with the composition of preserved garnet cores and their inclusions, in order to verify the compatibility of the two compositions. This compatibility supports the textural observations that the "*atollization*" process took place during D2 and was the result of the transformation of garnet cores become instable at the new PT condition, and possibly substituted by a new, more stable assemblage only along fractures, pathways of fluid circulation. Models allow to predict that the four analyzed micro-domains from the three modeled samples share a common evolution, and preserve evidence of a prograde transformation from upper greenschist to amphibolite facies (D1 to D2). Peak conditions are represented by late-D1 parageneses and indicate P = 0.72-0.82 GPa and T = 565-585 °C (Figure 11). Successively a decrease of pressure associated with a slight temperature increase (P = 0.46-0.70 GPa, T = 500-600 °C), contemporaneous to recrystallization, was attained during the former stages of exhumation at the end of the Variscan orogeny (Figure 16).

Conclusions

The aim of this work is to constrain the different stages of re-equilibration witnessed by the selected samples during their PT evolution by means of the image assisted analysis and, at the same time, to ascertain which one of the atollization mechanisms suggested in literature can be properly invoked. Selected garnet micaschist nearby Santa Lucia del Mela record a prograde evolution to amphibolite facies conditions preserved in garnet cores, followed by decompression associated with slight heating to lower amphibolite up to greenschist facies (Figure 16). This evolution was constrained using thermodynamic modelling of the equilibrium assemblages and isopleths intersections with the software perplex in volumes in which microstructural evidences indicate the attainment of equilibrium.

The microstructural analysis supplemented by the use of assisted image analysis allowed the recognition of two stages of a single metamorphic cycle. The first one was responsible for the garnet formation and can be subdivided in an early stage represented by inclusion-rich garnet cores, followed by a late

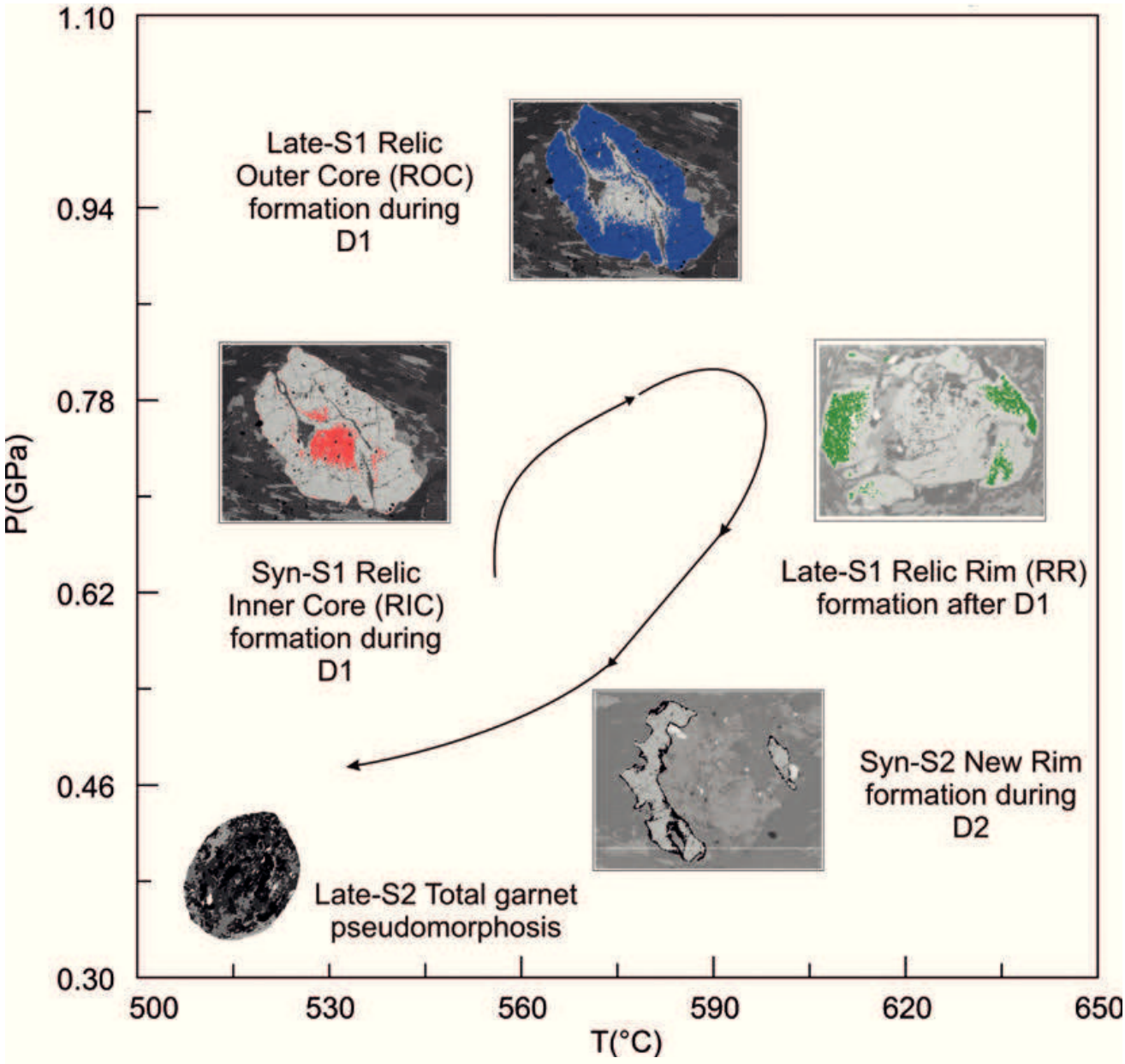

Figure 16. Reconstruction of the final P-T path reporting the sequential stages of atoll-garnet formation.

stage of euhedral to sub-euhedral garnet overgrowth almost without of inclusions. The garnet core grew during D1 accompanied by simple shear and continued to growth statically before being wrapped by the S2 foliation. The second stage, also developed during a non-coaxial deformational regime is responsible of the well developed crenulation schistosity as well as of the garnet inner core breakdown with the formation of the atoll shaped structure.

It is likely that in our case the already suggested hypotheses implying selective dissolution of the cores of pre-existing garnets may be compatible with the following evidences: 1) the resorption of a Sps-rich core and the successive formation of a Mn-rich garnet, related

to fluid circulation associated with garnet-core dissolution, and concentrated along fractures; 2) the composition of the last garnet, corresponds to the sum of the relic Mn-rich inner core plus the overgrowing zone of the new rim; 3) in the third stage of atollization the presence of this new rim is recognizable also in the inner portion of the relic garnet, which clearly points to the fact that the observed chemical pattern cannot be the result of a multiple coalescence nor a change in the stoichiometry of the reactions that lead to the transition from a poykilitic core to an euhedral rim devoid of inclusions.

Acknowledgements

This work has benefited from the constructive suggestions of several colleagues among which P. Fiannacca and R. Punturo. Special thanks to Antonio Pezzino for his precious guide on the geology and petrology of the Peloritani Mountains and to Giuseppe Guzzetta for his meticulous and critical reading of the paper. Richard Spiess, Martin Robyr and María D. Ruiz Cruz meticulous reviews improved the original manuscript and gave us many more occasions of discussion.

References

Amodio Morelli L., Bonardi G., Colonna V., Dietrich D., Giunta G., Ippolito F., Liguori V., Lorenzoni S., Paglionico A., Perrone V., Piccarreta G., Russo M., Scandone P., Zanettin Lorenzoni E. and Zuppetta A. (1976) - L'Arco Calabro-Peloritano nell'orogene appenninico-maghrebide. *Memorie della Società Geologica Italiana*, 17, 1-60.

Ague J.J. and Carlson W.D. (2013) - Metamorphism as Garnet Sees It: The kinetics of nucleation and growth, equilibration, and diffusional relaxation. *Elements*, 9, 439-445.

Angì G., Cirrincione R., Fazio E., Fiannacca P., Ortolano G. and Pezzino A. (2010) - Metamorphic evolution of preserved Hercynian crustal section in the Serre Massif (Calabria-Peloritani Orogen, southern Italy). *Lithos*, 115, 237-262.

Arenas R., Abati J., Martinez Catalan J.R., Diaz Garcia F. and Rubio Pascual F.J. (1997) - P-T evolution of eclogites from the Agualada Unit (Ordenes Complex, northwest Iberian Massif, Spain): Implications for crustal subduction. *Lithos,* 40, 221-242.

Atherton M.P. and Edmunds W.M. (1966) - An electron microprobe study ofsome zoned garnets from metamorphic rocks. *Earth Planetary Science Letters,*1, 185-193.

Atzori P. and D'Amico C. (1972) - Rapporti tra gneiss occhiadini e filladi a Savoca (Peloritani, Sicilia). *Mineralogica et Petrographica Acta*, 18, 83-96.

Bonnet N. (1995) - Processing of images and image series: A tutorial review for chemical microanalysis. *Mikrochimica Acta,* 120, 195-210.

Bonnet N. (1998) - Multivariate statistical methods for the analysis of microscope image series: applications in material science. *Journal of Microscopy,* 190, 2-18.

Cella F., Cirrincione R., Critelli S., Mazzoleni P., Pezzino A., Punturo R., Fedi M. and Rapolla A. (2004) - Gravity Modeling in Fold-Thrust Belts: An Example from the Peloritani Mountains, Southern Italy. *International Geological Review*, 46 (11), 1042-1050.

Cirrincione R. and Pezzino A. (1991) - Caratteri strutturali dell'evento Alpino nella serie mesozoica di Alì e nell'Unità metamorfica di Mandanici (Peloritani Orientali). *Memorie della Società Geologica Italiana,* 47, 263-272.

Cirrincione R., Atzori P. and Pezzino A.(1999) - Sub-greenschist facies assemblages of metabasites in South-Eastern sector of Peloritani range. *Mineralogy and Petrology*, 67, 193-212.

Cirrincione R., Ortolano G., Pezzino A. and Punturo R. (2008) - Poly-orogenic multi-stage metamorphic evolution inferred via P–T pseudosections: an example from Aspromonte Massif basement rocks (Southern Calabria, Italy). *Lithos*, 103, 466-502.

Cirrincione R., Fazio E., Ortolano G., Pezzino A. and Punturo R. (2012) - Fault-related rocks as a tool for

the comprehension of structural and metamorphic evolution of an accretionary wedge in a collisional belt (Peloritani Mountains, NE Sicily). *International Geological Review,* 54, 940-956.

Cheng H., Nakamura E., Kobayashi K. and Zhou Z. (2007) - Origin of atoll garnets in eclogites and implications for the redistribution of trace elements during slab exhumation in a continental subduction zone. *American Mineralogist*, 92, 1119-1129.

Connolly J.A.D. (2005) - Computation of phase equilibria by linear programming: a tool for geodynamic modeling and its application to subduction zone decarbonation. *Earth Planetary Science Letters,* 236, 524-541.

Connolly J.A.D. and Petrini K. (2002) - An automated strategy for calculation of phase diagram sections and retrieval of rock properties as a function of physical conditions. *Journal of Metamorphic Geology,* 20, 697-708.

Cooper A.F. (1972) - Progressive metamorphism of metabasic rocks from the Haast Schist Group of southern New Zealand. *Journal of Petrology*, 13, 457-492.

de Capitani C. and Petrakakis K. (2010) - The computation of equilibrium assemblage diagrams with Theriak/Domino software. *American Mineralogist*, 95 (7), 1006-1016.

Dobbs H.T., Peruzzo L., Seno F., Spiess R. and Prior D.J. (2003) - Unravelingthe Schneeberg garnet puzzle. A numerical model of multiple nucleation and coalescence. *Contriution of Mineralogy and Petrology,* 146, 1-9.

Cossio R. and Borghi A. (1998) - PETROMAP: MS-DOS software package 1 for quantitative processing of X-ray maps of zoned minerals. *Computers and Geosciences*, 24, 797-803.

Cossio R., Borghi A. and Ruffini R. (2002) - Quantitative modal determination of geological samples based on X-ray multielemental map acquisition. *Microscopy and Microanalysis,* 8, 139-149.

Dainelli N., Bonechi F., Spagnolo M. and Canessa A. (2010) - Cartografia numerica: Manuale pratico per l'utilizzo dei GIS. Dario Flaccovio, Palermo, 372 pp.

De Andrade V., Vidal O., Lewin E., O'Brien P. and Agard P. (2006) - Quantification of electron microprobe compositional maps of rock thin sections: an optimized method and examples. *Journal of Metamatical Geol*ogy, 24, 655-668.

Evans T.P. (2004) - A method for calculating effective bulk composition modification due to crystal fractionation in garnet-bearing schists: implications for isopleths thermobarometry. *Journal of Metamorphic Geology,* 22, 547-557.

Faryad S.W., Klápová H. and Nosál L. (2010) - Mechanism of formation of atoll garnet during high-pressure metamorphism. *Mineralogical Magazine,* 74, 111-126.

Ferla P. (2000) - A model of continental crustal evolution in the geological history of the Peloritani Mountains (Sicily). *Memorie della Società Geologica Italiana*, 55, 87-93.

Festa V., Messina A., Paglionico A., Piccarreta G. and Rottura A. (2004) - Pre-Triassic history recorded in the Calabria-Peloritani segment of the Alpine chain, southern Italy. An overview. *Periodico di Mineralogia*, 73, 57-71.

Fiannacca P., Williams I.S., Cirrincione R. and Pezzino A. (2008) - Crustal contributions to Late-Hercynian peraluminous magmatism in the Southern Calabria-Peloritani Orogen, Southern Italy: petrogenetic inferences and the Gondwana connection. *Journal of Petrology,* 49, 1497-1514.

Fiannacca P., Lo Po' D., Ortolano G., Cirrincione R. and Pezzino A. (2012) - Thermodynamic modeling assisted by multivariate statistical image analysis as a tool for unraveling metamorphic P T-d evolution: an example from ilmenite-garnet-bearing metapelite of the Peloritani Mountains, Southern Italy. *Mineralogy and Petrology,* 106 (3-4), 151-171.

Flesche H., Nielsen A.A. and Larsen R. (2000) - Supervised mineral classification with semi-automatic training and validation set generation in scanning electron microscope energy dispersive spectroscopy images of thin sections. *Mathematical Geology* 32, 337-366.

Friel J.J. and Lyman C.E. (2006) - X-ray mapping in electron-beam instruments. *Microscopy and Microanalysis*, 12, 2-25.

Hibraim A.A. (2012) - Formation of Atoll Garnets in the Banded Iron Formation of Maru Schist Belt. *American International Journal of Contemporary Research,* 2 (5), 210-221.

Holland T.J.B. and Powell R. (1998) - An internally consistent thermodynamic data set for phases of petrological interest. *Journal of Metamorphic Geology*, 16, 309-343.

Holland T., Baker J. and Powell R. (1998) - Mixing

properties and activity-composition relationships of chlorites in the system MgO-FeO-Al_2O_3-SiO_2-H_2O. *European Journal of Mineralogy*, 10, 395-406.

Hollister L.S. (1966) - Garnet zoning: an interpretation based on the Rayleigh fractionation model *Science*, 154, 1647-1651.

Homam S.M. (2003) - Formation of atoll garnet in the Ardara aureole, NW Ireland. *Journal of Sciences, Islamic Republic of Iran*, 14, 247-258.

Homam S.M. (2006) - The occurrence and origin of atoll garnet in hornblende schists from the contact aureole of the Mashhadgranite, NE Iran. *Iranian Journal of Science and Technology*, 30, 127-132.

Lanari P., Vidal O., De Andrade V., Dubacq B., Lewin, E., Grosch E. and Schwartz S. (2014) - XMapTools: a MATLAB©-based program for electron microprobe Xray image processing and geothermobarometry. *Computers and Geosciences*, 62, 227-240.

Launeau P., Cruden A.R. and Bouchez J.L. (1994) - Mineral recognition in digital images of rocks: a new approach using multichannel classification. *Canadian Mineralogist*, 32, 919-933.

Messina A., Somma R., Macaione E., Carbone G. and Careri G. (2004) - Peloritani Continental Crust Composition (Southern Italy): geological and petrochemical evidence. *Bollettino della Società Geologica Italiana*, 123, 405-441.

Newton R.C., Charlu T.V. and Kleppa O.J. (1980) - Thermochemistry of the high structural state plagioclases. *Geochemica et Cosmochimica Acta,* 44, 933-41.

Ortolano G., Zappalà L., Mazzoleni P., (2014) - X-Ray Map Analyzer: a new ArcGIS® based tool for the quantitative statistical data handling of X-ray maps (Geo- and material-science applications). *Computers and Geosciences*, 72, 49-64.

Passchier C.W. and Trouw R.A.J. (1998) - Microtectonics. Springer, Berlin, 289 pp.

Pezzino A., Pannucci S., Puglisi G., Atzori P., Ioppolo S. and Lo Giudice A. (1990) - Geometry and metamorphic environment of the contact between the Aspromonte-Peloritani Unit (Upper Unit) and Madonna dei Polsi Unit (Lower Unit) in the central Aspromonte area (Calabria). *Bollettino della Società Geologica Italiana,* 109, 455-469.

Piluso E., Cirrincione R. and Morten L. (2000) - Ophiolites of the Calabrian Peloritan Arc and their relationships with the crystalline basement (Catena Costiera and Sila Piccola, Calabria, Southern Italy) in GLOM 2000 Excursion Guide-Book. *Ofioliti*, 25 (2), 117-140.

Puglisi G. and Pezzino A. (1994) - Metamorphism in the central Aspromonte area: geological, mineralogical and petrogenetic relationships. *Periodico di Mineralogia,* 63, 153-168.

Richard L.R. (1995) - Minpet: Mineralogical and Petrological Data Processing System, version 2.02. MinPet Geological Software, Quebec, Canada.

Robyr M., Vonlanthen P., Baumgartner L.P. and Grobety B. (2007) - Growth mechanism of snowball garnets from the Lukmanier Pass area (Central Alps, Switzerland): A combined μCT/EPMA/EBSD study. *Terra Nova*, 19 (4), 240-244.

Robyr M., Carlson W.D., Passchier C. andVonlanthen P. (2009) - Microstructural, chemical and textural records during growth of snowball garnet. *Journal of Metamorphic Geology*, 27, 423-437.

Robyr M., Darbellay B. and Baumgartner L.P. (2014) - Matrix-dependent garnet growth in polymetamorphic rocks of the Sesia zone, Italian Alps. *Journal of Metamorphic Geology,* 32, 3-24.

Rottura A., Bargossi G.M., Caironi V., Del Moro A., Maccarrone E.,Macera P., Paglionico A., Petrini R., Piccarreta G. and Poli G. (1990) - Petrogenesis of contrasting Hercynian granitoids from the Calabrian Arc, southern Italy. *Lithos,* 24, 97-119.

Ruiz Cruz M.D. (2011) - Origin of atollgarnet in schists from the Alpujarride Complex (Central zone of the Betic Cordillera, Spain): Implications on the P-T evolution. *Mineralogy and Petrology*, 101, 3-4, 245-261.

Smellie J.A.T. (1974) - Formation of atoll garnets from the aureole of the Ardara pluton, Co. Donegal, Ireland. *Mineralogical Magazine,* 39, 878-888.

Smellie J.A.T. (1989) - Atoll garnet. In: Browes D.R. (Ed.) The Encyclopedia of Igneous and Metamorphic Petrology. Van Nostrand Reinhold, New York, 42-43.

Spear F.S. (1993) - Metamorphic Phase Equilibria and Pressure-Temperature-Time Paths. Mineralogical Society of America, Washington, D.C. 799 pp.

Spiess R., Peruzzo L., Prior D.J. and Wheeler J. (2001) - Development of garnet porphyroblasts by multiple nucleation, coalescence and boundary misorientation driven rotations. *Journal of Metamorphic Geology,* 19, 269-290.

Tajcmanová L., Connolly J.A.D. and Cesare B. (2009)

- A thermodynamic model for titanium and ferric iron solution in biotite. *Journal of Metamorphic Geology*, 27, 153-64.

Tinkham D., Zuluaga C.A. and Stowell, H.H. (2001) - Metapelite phase equilibria modeling in MnNCKFMASH: The effect of variable Al_2O_3 and MgO/(MgO+FeO) on mineral stability. *Geological Materials Research*, 3 (1), 1-42.

Tracy R.J. (1982) - Compositional zoning and inclusions in metamorphic minerals. *Reviews in Mineralogy*, 10, 355-397.

von Raumer J.F., Stampfli G.M., Borel G. and Bussy F. (2002) - The organization of pre-Variscan basement areas at the north-Gondwanan margin. *International Journal of Earth Sciences,* 91, 35-52.

Zuluaga C.A., Stowell H.H. and Tinkham D.K. (2005) - The effect of zoned garnet on metapelite pseudosection topology and calculated metamorphic P-T paths. *American Mineralogist,* 90, 1619-1628.

Submitted, May 2014 - Accepted, September 2014

Table A1. Representative mineral analysis of garnet.

Sample	Me17			Sam3			
Zone	RIC	ROC	NR	RIC	ROC	RR	NR
SiO_2	37.73	37.75	37.66	37.85	37.59	38.45	37.66
TiO_2	0.21	0.12	0.20	0.21	0.17	0.18	0.2
Al_2O_3	21.18	21.13	20.78	21.23	21.27	21.30	20.78
Cr_2O_3	0.12	0.12	0.30	0.18	0.06	0.12	0.3
FeO_{Tot}	26.48	30.37	28.51	26.05	30.19	28.56	28.51
MnO	4.25	1.81	7.22	4.64	2.38	3.65	7.22
MgO	1.39	3.12	2.41	1.39	2.77	2.14	2.41
CaO	7.86	4.91	2.80	8.20	5.02	5.37	2.8
Total	99.22	99.33	99.88	99.75	99.45	99.77	99.88
Si	3.044	3.030	3.041	3.036	3.02	3.086	3.041
Al^{IV}	0	0	0	0	0	0	0
Sum_T	3.044	3.030	3.041	3.036	3.02	3.086	3.041
Al^{VI}	2.012	1.997	1.976	2.006	2.012	2.013	1.976
Fe^3	0	0	0	0	0	0	0
Ti	0.013	0.007	0.012	0.013	0.010	0.011	0.012
Cr	0.008	0.008	0.019	0.011	0.004	0.008	0.019
Sum_A	2.033	2.012	2.007	2.03	2.026	2.032	2.007
Fe^2	1.787	2.039	1.925	1.748	2.028	1.917	1.925
Mg	0.167	0.373	0.290	0.166	0.332	0.256	0.290
Mn	0.29	0.123	0.494	0.315	0.162	0.248	0.494
Ca	0.679	0.422	0.242	0.705	0.432	0.462	0.242
Sum_B	2.924	2.957	2.952	2.934	2.954	2.883	2.952
Sum_Cat	8	8	8	8	8	8	8
Number of O_2	12	12	12	12	12	12	12
Alm	61.109	68.936	65.232	59.566	68.661	66.494	65.232
Grs	22.846	13.892	7.234	23.438	14.433	15.622	7.234
Prp	5.718	12.624	9.829	5.666	11.230	8.882	9.829
Sps	9.934	4.161	16.731	10.746	5.482	8.607	16.731
Uvr	0.393	0.386	0.973	0.584	0.193	0.396	0.973

Appendix A

Representative mineral chemistry analysis for garnet, ilmenite, plagioclase, biotite, white mica and chlorite.

Table A2. Representative mineral analysis of ilmenite and plagioclase.

	Ilmenite		Plagioclase			
Sample	Me17		Me17		Sam3	Me02
Zone	Inclusion	Within atoll	Matrix	Within atoll	Within atoll	Pseudomorphosis
SiO_2	0.00	0.00	62.08	59.77	57.29	65.11
TiO_2	51.51	54.02	0.00	0.00	0.00	0.00
Al_2O_3	0.00	0.00	23.98	25.53	27.68	22.08
FeO_{Tot}	46.55	43.3	0.00	0.00	0.00	0.00
MnO	1.29	2.52	0.00	0.00	0.00	0.00
MgO	0.64	0.16	0.00	0.00	0.00	0.00
CaO	0.00	0.00	8.13	7.12	7.42	2.98
Na_2O	0.00	0.00	5.16	7.16	6.68	8.86
K_2O	0.00	0.00	0.00	0.00	0.00	0.00
Total	100	100	99.35	99.58	99.21	99.21
Si	0.000	0.000	2.755	2.668	2.574	2.872
Al	0.000	0.000	1.253	1.342	1.464	1.147
Fe^3	0.000	0.000	0.000	0.000	0.000	0.000
Ti	1.962	2.034	0.000	0.000	0.000	0.000
Fe^2	1.972	1.813	0.000	0.000	0.000	0.000
Mg	0.048	0.012	0.000	0.000	0.000	0.000
Ca	0.000	0.000	0.387	0.340	0.357	0.141
Mn	0.055	0.107	0.000	0.000	0.000	0.000
Na	0.000	0.000	0.444	0.620	0.594	0.758
K	0.000	0.000	0.000	0.000	0.000	0.000
Sum_Cat	4.037	3.966	4.839	4.97	4.989	4.931
Ab			53.40	64.6	62.5	84.3
An			46.60	35.4	37.5	15.7

Table A3. Representative mineral analysis of biotite, white mica and chlorite.

	biotite				white mica		chlorite	
Sample	Me17		Sam3	Me02	Me17		Me02	
Zone	Matrix	Within atoll	Within atoll	Pseudomorphosis	Matrix	Within atoll	Matrix	Pseudomorphosis
SiO_2	36.44	41.71	39.65	39.30	48.3	47.56	26.68	28.43
TiO_2	1.53	0.92	0.9	0.27	0.67	0.67	0.00	0.00
Al_2O_3	19.59	22.38	22.86	20.8	34.14	36.32	23.35	20.88
FeO_{Tot}	17.85	9.45	14.77	19.27	0.96	0.87	21.85	24.45
MnO	0.14	0.09	0.2	0.00	0.00	0.00	0.00	0.00
MgO	11.17	14.02	13.62	13.04	1.24	0.72	16.82	15.44
Na_2O	0.20	0.44	0.82	0.00	0.90	1.21	0.00	0.00
K_2O	8.42	7.13	3.04	4.36	9.43	9.04	0.00	0.00
Total	95.33	96.14	95.86	97.05	95.64	96.39	88.70	89.20
Si	2.849	3.031	2.911	2.928	3.172	3.094	5.413	5.800
Al^{IV}	1.151	0.969	1.089	1.071	0.828	0.906	2.587	2.220
Al^{VI}	0.653	0.947	0.888	0.756	1.818	1.877	2.993	2.817
Ti	0.090	0.050	0.050	0.015	0.033	0.003	0.000	0.000
Fe_2	1.167	0.574	0.907	1.205	0.053	0.047	3.708	4.172
Mg	1.302	1.519	1.491	1.454	0.121	0.070	5.088	4.696
Mn	0.009	0.006	0.012	0.00	0.000	0.000	0.000	0.000
Na	0.030	0.062	0.117	0.00	0.115	0.153	0.000	0.000
K	0.839	0.661	0.285	0.414	0.790	0.750	0.000	0.000
Sum_Cat	8.090	7.819	7.750	7.846	6.924	6.930	19.789	19.685
Number of O_2	12	12	12	12	12	12	36	36
XMg	0.53	0.73	0.62	0.54	0.70	0.60	0.58	0.53

Appendix B

Graphical representation of the sequence of the image analysis procedure: BSE (Back Scattered Electron image); PCA1 (Principal Component Analysis for the first analytical cycle); MLC1/2 (Maximum Likelihood Classification for the first and second analytical cycle, respectively).

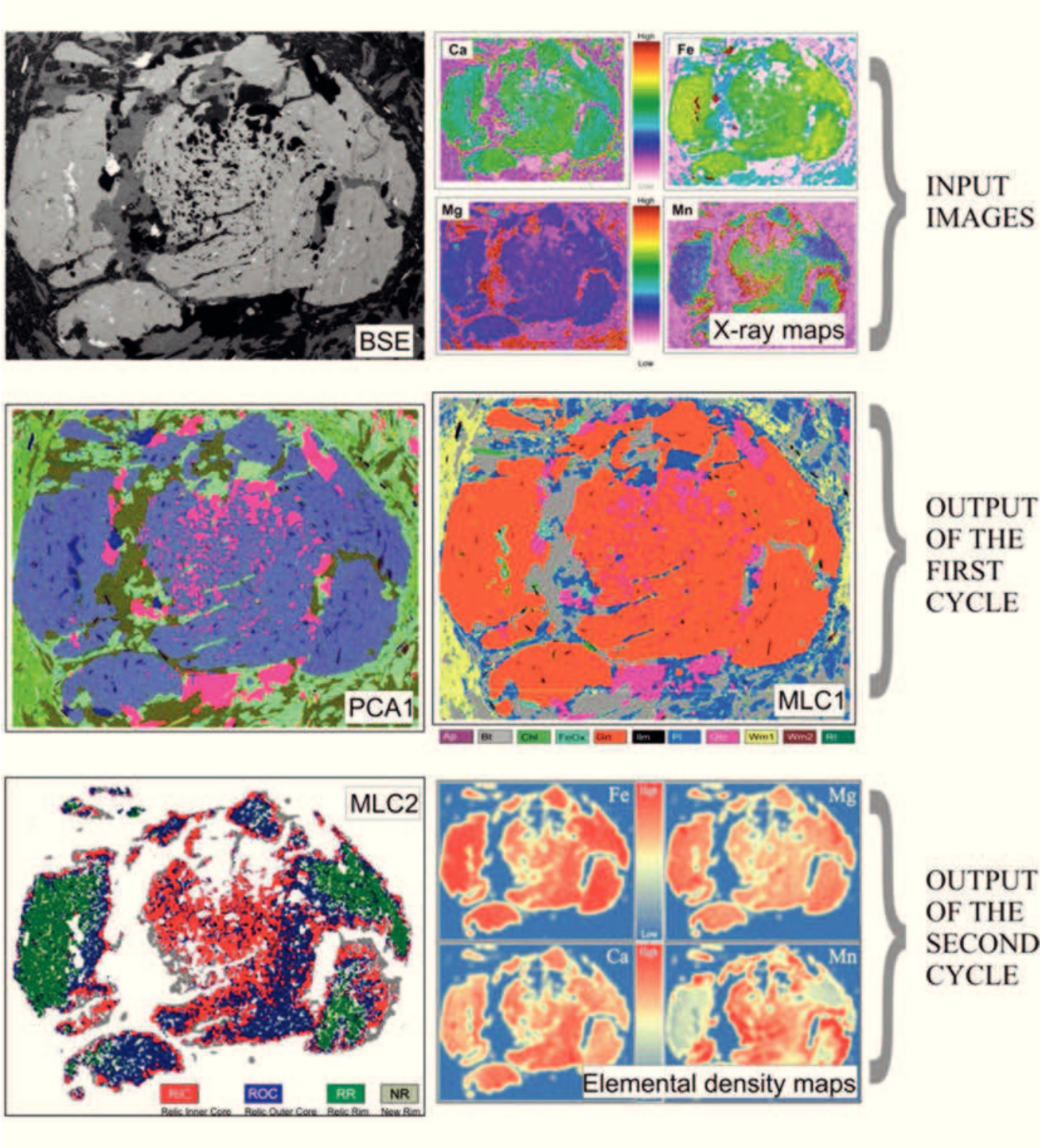

Appendix C

Quantitative extrapolation of the volume percentage of the inclusions within first and second garnet growth generation in the samples Me17 (microdomain a) and sample Sam3 by means of map algebra functions.

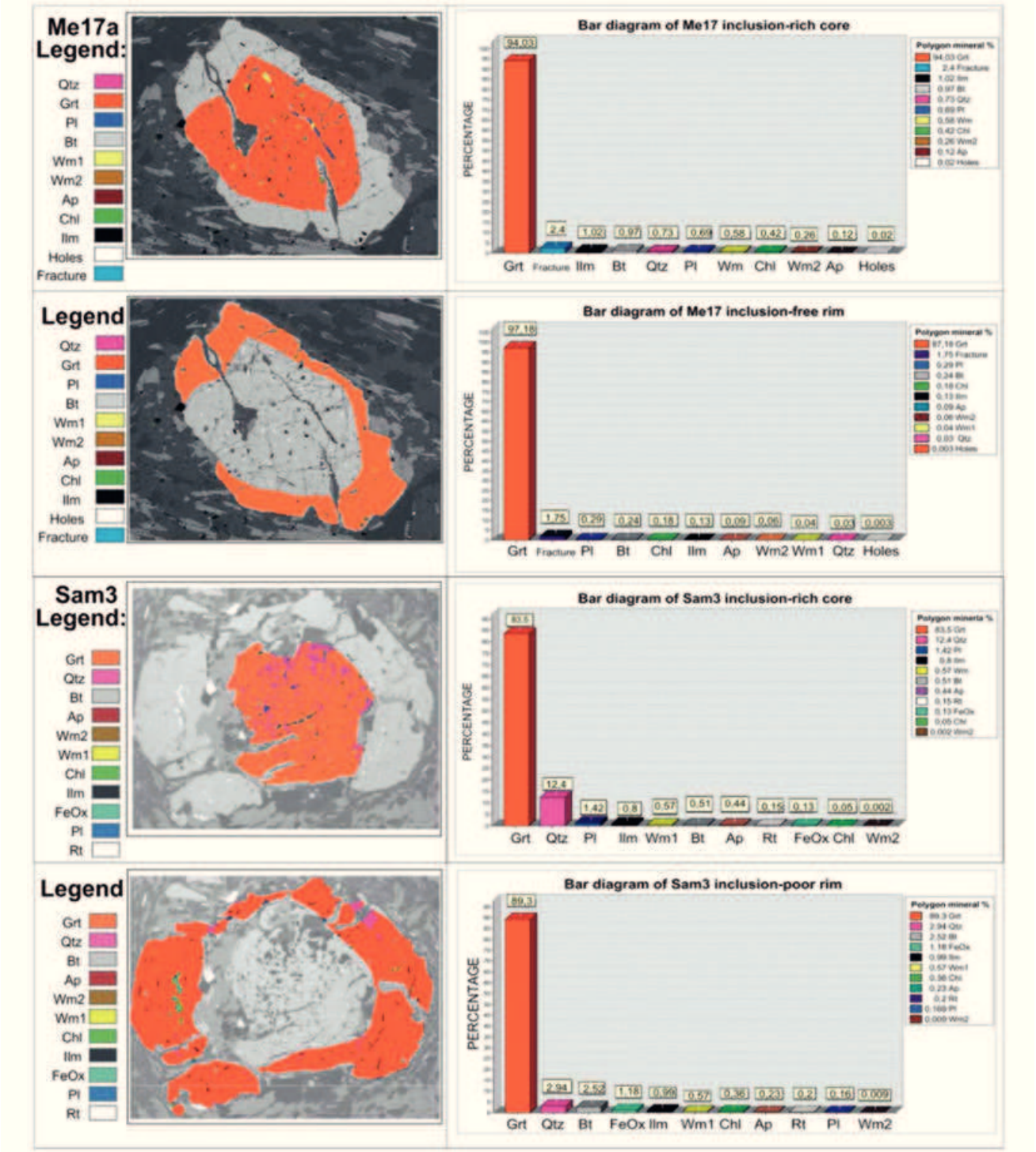

Appendix D

Compositional ranges and ternary diagram of the garnet growth stages for each three selected garnet microdomain: RIC (Relic Inner Core - red); ROC (Relic Outer Core - blue); RR (Relic Rim - green); NR (New Rim - grey).

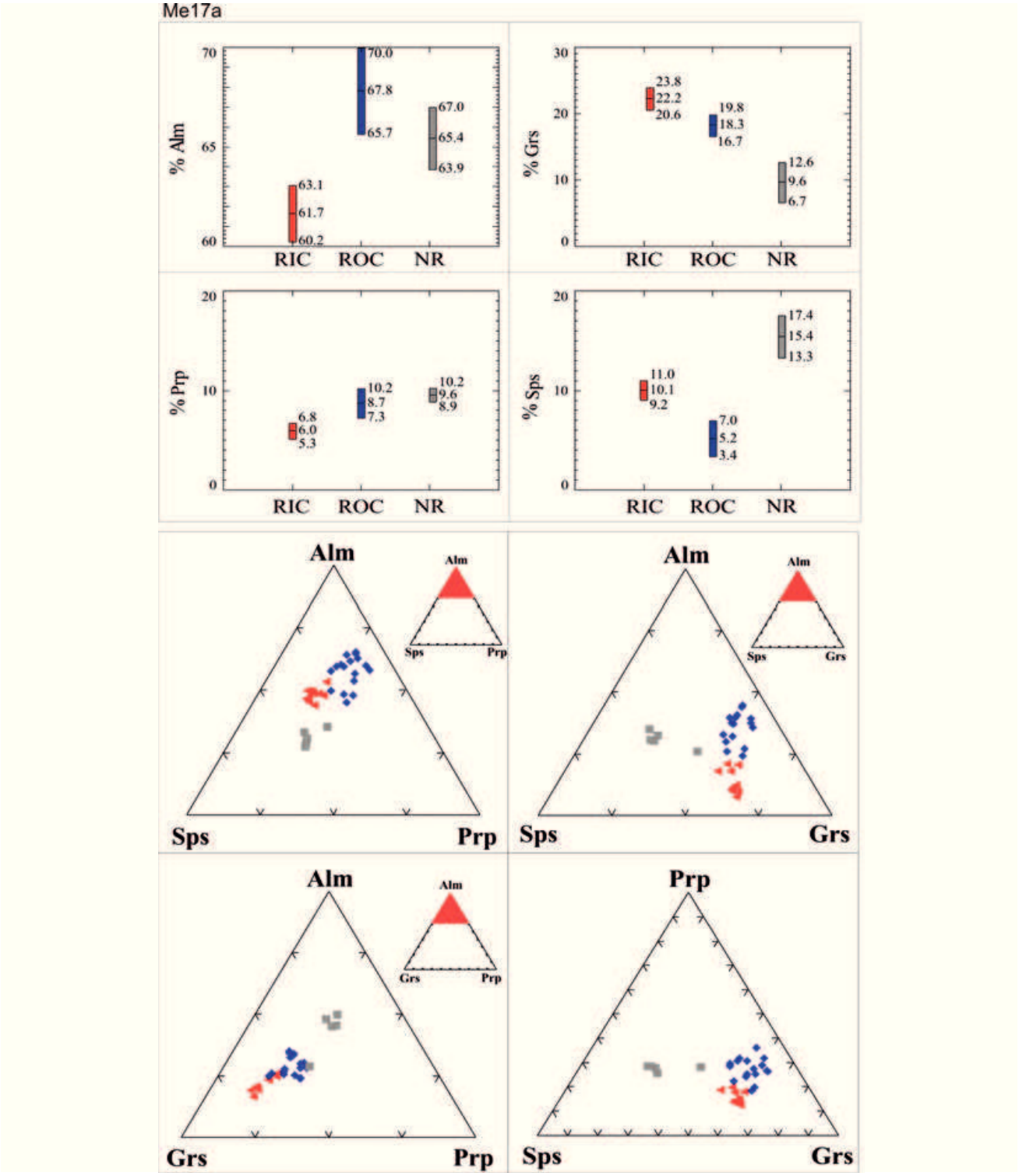

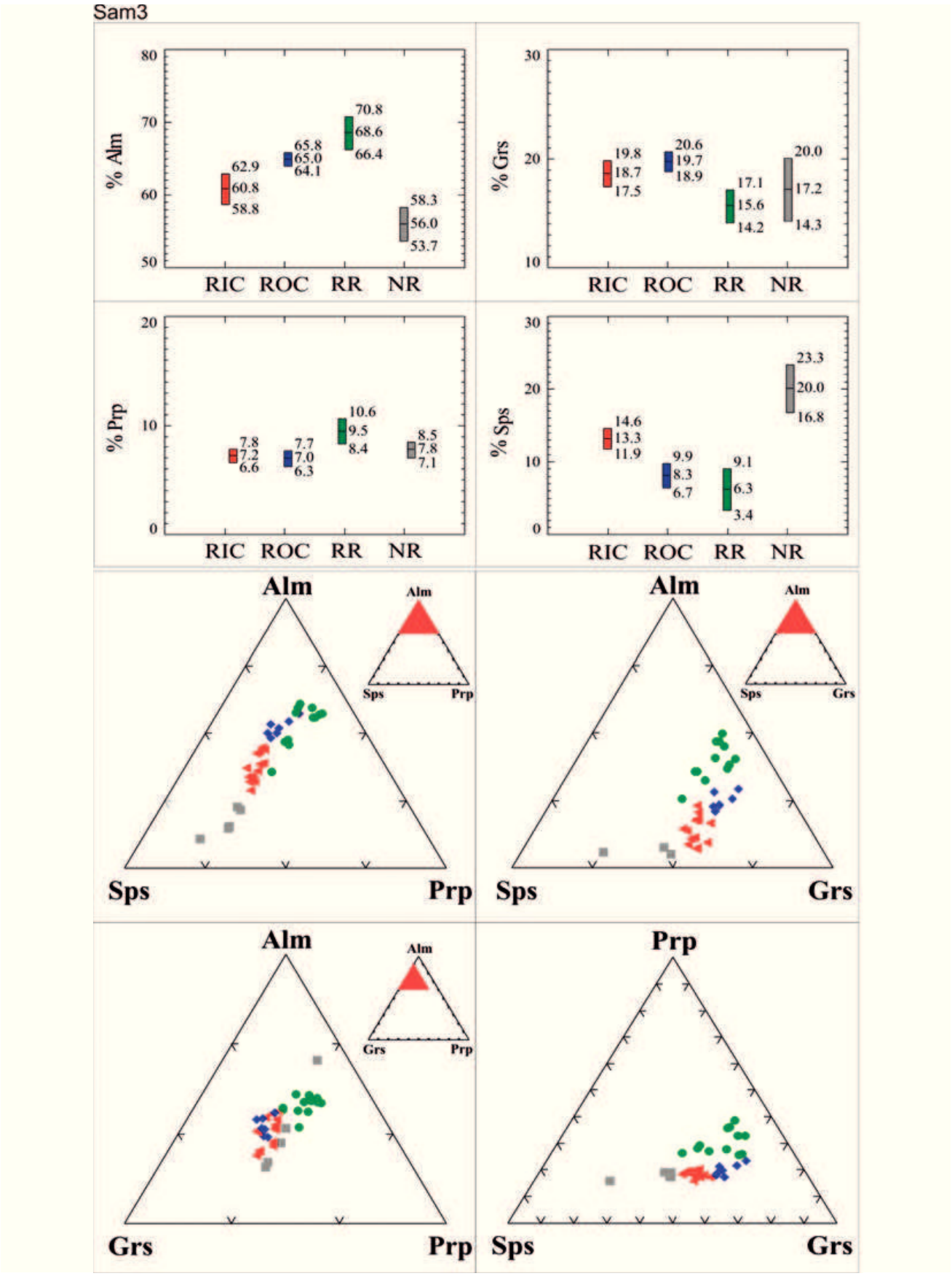
Sam3
% Alm
80
70
60
50
62.9
60.8
58.8
65.8
65.0
64.1
70.8
68.6
66.4
58.3
56.0
53.7
RIC ROC RR NR
% Grs
30
20
10
19.8
18.7
17.5
20.6
19.7
18.9
17.1
15.6
14.2
20.0
17.2
14.3
RIC ROC RR NR
% Prp
20
10
0
7.8
7.2
6.6
7.7
7.0
6.3
10.6
9.5
8.4
8.5
7.8
7.1
RIC ROC RR NR
% Sps
30
20
10
0
14.6
13.3
11.9
9.9
8.3
6.7
9.1
6.3
3.4
23.3
20.0
16.8
RIC ROC RR NR
Alm
Sps
Prp
Alm
Sps
Prp
Alm
Sps
Grs
Alm
Sps
Grs
Alm
Grs
Prp
Grs
Prp
Prp
Sps
Grs

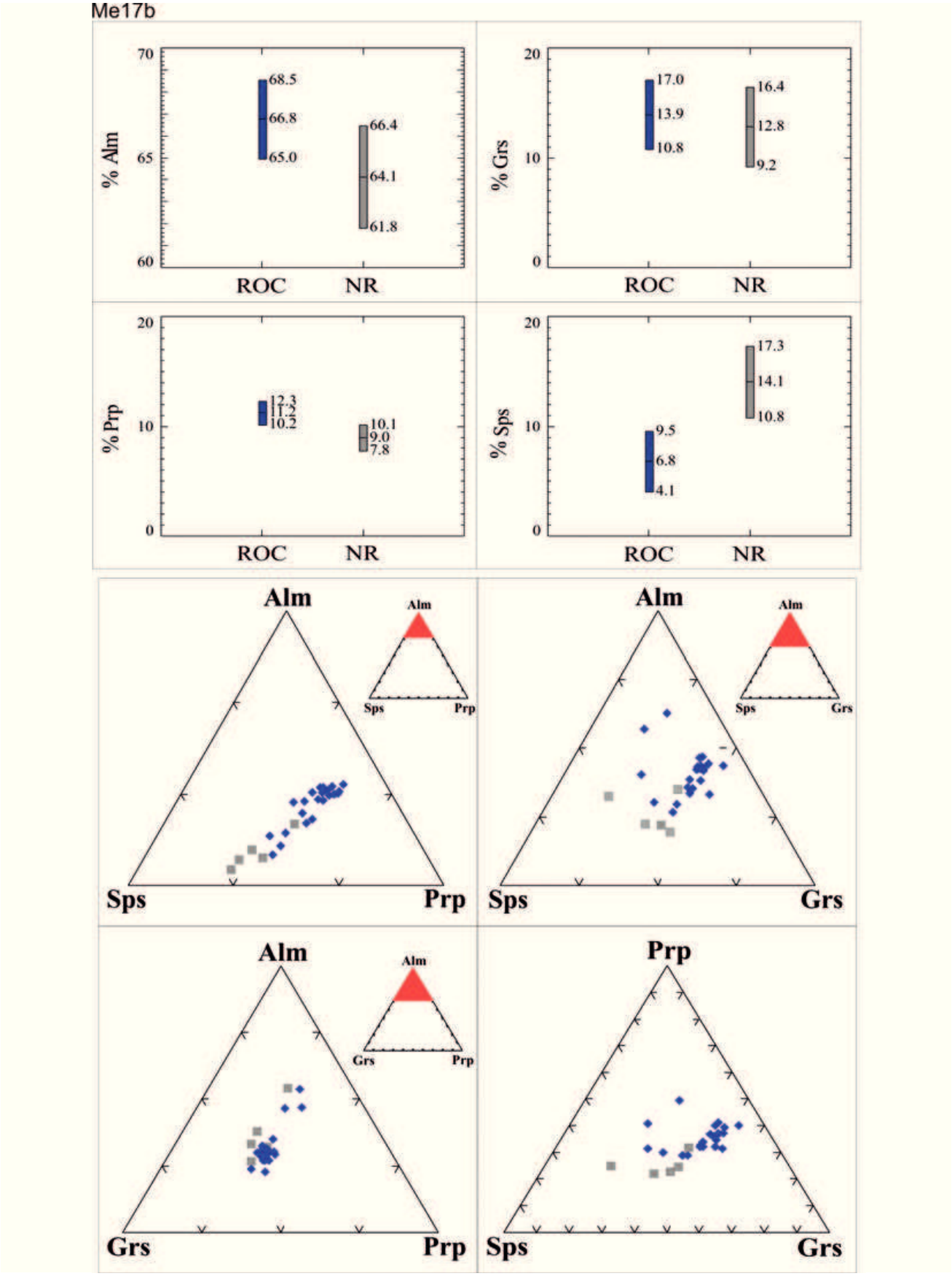
Me17b
% Alm
70
65
60
68.5
66.8
65.0
66.4
64.1
61.8
ROC
NR
% Grs
20
10
0
17.0
13.9
10.8
16.4
12.8
9.2
% Prp
12.3
11.2
10.2
10.1
9.0
7.8
% Sps
9.5
6.8
4.1
17.3
14.1
10.8
Alm
Sps
Prp
Grs